Enhancing Neutral Propellant Flow Uniformity in Hall Thrusters via Anode Design

Daniel Roberts

A thesis
submitted in partial fulfillment of the
requirements for the degree of

Master of Science in Aeronautics and Astronautics

University of Washington

2024

Committee:

Justin Little

Uri Shumlak

Program Authorized to Offer Degree:
Aeronautics & Astronautics

University of Washington

Abstract

Enhancing Neutral Propellant Flow Uniformity
in Hall Thrusters via Anode Design

Daniel Roberts

Chair of the Supervisory Committee:
Justin Little
Aeronautics & Astronautics

The uniformity of propellant gas flow in the discharge channel of Hall thrusters is a crucial factor for thruster performance. Uneven particle flux to the ionization region results in asymmetric thrust vectors, diminished propellant ionization, and decreased total efficiency. In this work, the gas density profiles within the ACME Hall thruster discharge channel were characterized for four unique anode designs with a modified fast ionization gauge. Additive manufacturing was used to develop anode models with complex internal baffles that aimed to increase flow uniformity and decrease axial flow velocity. Normalized, fine resolution azimuthal measurements were made at 4-5 axial locations, and empirical fits were generated to quantify the evolution of pressure uniformity as a function of axial distance from the anode. Results were compared to the NASA standard acceptance criteria of $\leq 5\%$ absolute deviation (α) and $\leq 10\%$ peak-to-peak deviation (μ) from the mean pressure at the axial midpoint between the anode and thruster exit plane. The original ACME anode met the NASA acceptance criteria, despite observed asymmetries in erosion and plasma density, with $\alpha = 2.57\%$ and $\mu = 4.23\%$. Two novel anode designs improved flow uniformity with fit functions predicting $\alpha = 0.47\%$ and $\alpha = 0.87\%$ at the criteria location. Upcoming ACME performance testing will quantify the effect that these gains in neutral azimuthal uniformity have on thruster efficiency.

TABLE OF CONTENTS

LIST OF FIGURES

LIST OF TABLES

ACKNOWLEDGMENTS

I would like to express my immense gratitude to my advisor, Justin Little, for your years of guidance and mentorship. Ever since you let me into your lab as an undergrad, I have been on an endless, wonderful journey of realizing how much I didn't and still don't know. Having the opportunity to do both research and teaching assistantships with you did not only elevate my skills and confidence considerably, but also freed my graduate years from the financial strain that many students are burdened with. I will be emulating your approaches to teaching, problem solving, and cultivating work environments in my future leadership roles. Thank you for founding and welcoming me into the SPACE Lab.

It cannot be overstated just how much Peter Thoreau, Landon Bevier, and Curits Promislow have taught me. The three of you are inspirationally talented engineers and incredibly fun people to be around. While you have shown me how to do countless small technical tasks in the lab with tools, mechanisms, and electronics, it is the macroscopic teachings that have truly impacted me.

Peter, you enlightened me to the mindset that any skill can be learned to address any problem. My current comprehension of nearly all things technical can trace back to you. While I doubt I'll ever achieve your insane level of work-hard-play-hard, I will be using it as a reference point for what is (humanly? I have my doubts...) possible. I look forward to our future outdoor adventures and thought-provoking discussions.

After just about every class session, I would head to the grad office and Landon would be there to translate what I'd just heard. Your ability to explain concepts in comprehensible terms is astounding. The passion you bring to science and engineering is infectious and I hope to become even a fraction as good of a teacher as you are.

I'll never forget the moments that Curtis forced me to think on the spot in Electric Propulsion Lab class, not due to embarrassment, but rather because it was in these moments when many plasma physics concepts finally clicked. Your electrical wizardry is shocking. Despite the cacophony of machines in the lab, your heart-warming laugh always seemed to drown them out.

In the family that is the SPACE Lab, Patrick Rae was my brother. I wouldn't say that grappling with difficult assignments from AMATH and plasma courses together was always a pleasure, but now I look back only fondly. Part of me is sad to not be continuing alongside you for a PhD of my own, but I'm glad to have been here for the beginning of yours. Thank you for your friendship and all our time together in AERB.

Thank you to my cousin, Dr. Anna Nelson, for being the academic and intellectual icon I have looked up to for my entire life.

Finally, I could not have willed myself out of bed each day if it were not for my love, Aisling. While this is partially because you made me coffee most mornings, it's mostly because I knew that each day I could get to experience the unparalleled joy of being by your side. Your kindness, humor, and overall radiance remind me of the beauty and value of life itself.

DEDICATION

To my parents,
for their endless support,
and for bestowing upon me
a profound passion for science.

Nomenclature

$(\ )_e$	Neutral Subscript	
$(\ )_i$	Ion Subscript	
$(\ )_n$	Electron Subscript	
α	Absolute Maximum Deviation From Mean	
Γ	Flux	$[\mathrm{m}^{-2}s{-}1]$
λ_i	Ionization Mean Free Path	[m]
$\langle \sigma_{ion} v_e \rangle$	Ionization Reaction Rate Coefficient	$[\mathrm{m}^3/s]$
μ	Peak-to-Peak Deviation From Mean	
ν	Total Collision Frequency	$[\mathrm{s}^{-1}]$
ω_c	Cyclotron Frequency	$[\mathrm{s}^{-1}]$
Ω_e	Hall Parameter	
σ_i	Ionization Cross Section	$[\mathrm{m}^2]$
σ	Standard Deviation	
$\tau_{\Delta P}$	Pressure Measurement Settling Time	[s]
T	Thrust	[N]

θ	Azimuthal Position	[°]
B	Magnetic Field	[T]
d	Diameter	[m]
E	Electric Field	[V/m]
e	Elementary Charge	[C]
F	Force	[N]
F_c	Centripetal Force	[N]
g_0	Standard Earth Gravitational Acceleration	[m/s^2]
I_d	Discharge Current	[A]
I_H	Hall Current	[A]
I_{ea}	Anode Electron Current	[A]
I_{sp}	Specific Impulse	[s]
J_{Hall}	Hall Current Density	[A/m^2]
k	Boltzmann Constant	[J/K, eV/K]
L	Characteristic Plasma Length Scale and/or Channel Length	[m]
L_p	Pitot Tube Length	[m]
m	Mass	[kg]

m_0	Initial Mass	[kg]
m_f	Final Mass	[kg]
n	Number Density	[m^{-3}]
P	Pressure	[Torr]
q	Electric Charge	[C]
r	Radius	[m]
r_L	Larmor Radius	[m]
S_{eff}	Effective Gas Conductance	[m^3/s]
T	Temperature	[K,eV]
T_e	Electron Temperature	[K,eV]
v	Velocity	[m/s]
V_b	Beam Voltage	[V]
V_d	Discharge Voltage	[V]
v_E	E×B Drift Velocity	[m/s]
v_e	Exhaust Velocity	[m/s]
V_{gauge}	Pressure Gauge Container Volume	[m^3]
v_{th}	Mean Thermal Velocity	[m/s]

w	Plasma Width	[m]
z	Axial Position	[m]

GLOSSARY

ACME: Adaptive-field Central-cathode Magnetically-shielded Electric

APAT: Anode Pressure Acceptance Test

DMLS: Direct Metal Laser Sintering

EP: Electric Propulsion

FDM: Fused Deposition Modeling

FIG: Fast Ionization Gauge

MJF: Multi Jet Fusion

PLA: Polylactic Acid

SPACE: Space Propulsion and Advanced Concepts Engineering

SPECTER: Space Propulsion Experiments and Cryogenic Test EnviRonment

Chapter 1

INTRODUCTION

1.1 Space Propulsion

The premise for this work all begins with the famous Tsiolkovsky rocket equation, derived from the conservation of momentum:

$$\Delta v = v_e \ln \frac{m_0}{m_f}$$

In words, it states that a vehicle's attainable change in velocity is equal to the product of propellant exhaust velocity and the natural log of the ratio of the initial spacecraft mass to its mass after ejecting propellant. This elegantly simple equation governs the travel of all spacecraft tyrannically, with Δv dictating not only how long a satellite may operate, but also how far humanity is ultimately capable of exploring the cosmos within a given time frame. The mass of celestial bodies and the laws of orbital mechanics set what are essentially astrodynamic prices on travel between any two locations, and the only accepted currency is Δv. While the minimum amount of Δv for a maneuver or mission is set in stone, the propulsion system ultimately dictates the amount of Δv a spacecraft of a given propellant mass fraction. The exit velocity v_e of propellant is also expressed as

$$v_e = I_{sp} g_0 \ ,$$

where I_{sp} is specific impulse and g_0 is standard gravitational acceleration. Technically defined as the ratio of thrust to the rate of propellant consumption, specific impulse is the primary measure of thrust efficiency that defines the amount of Δv achievable for a craft with a set m_0/m_f. Naturally, engineers have since the inception of astronautics tried to increase

and optimize the specific impulse for propulsion systems to boost the Δv for a payload, or increase the payload mass for a set mission.

1.2 Electric Propulsion and Hall Thrusters

Electric propulsion (EP) refers to systems that use electric energy to ultimately accelerate propellant away from a spacecraft, generating thrust and Δv. EP is a much smaller branch of the propulsion tree compared to the bough that is chemical propulsion: the well known and technologically mature form that extracts energy from chemical bonds to accelerate propellant supersonically with a nozzle. The primary interest in EP stems from the major gains in specific impulse that are achievable in comparison to chemical propulsion. Despite higher efficiencies, even the most powerful EP systems struggle to generate a fraction of the thrust attainable from chemical propulsion alternatives, and often require vacuum conditions for operation. These qualities carve out a niche for EP as the optimal choice for space missions that are not particularly time sensitive, such as robotic interplanetary science missions or satellite station-keeping.

While there are numerous types of EP systems, the most common in flight today is the Hall thruster. First developed in the 1960s by the Soviet Union, Hall thrusters are electrostatic thrusters that use electric fields to accelerate ionized propellant gas for thrust. Flight-model Hall thrusters have historically exhibited lower efficiency and specific impulse compared to ion thrusters, however their power density is superior and not limited by space-charge constraints [13] [32]. Although Hall thrusters now have a half century of use in their original form, only in the last decade or so have researchers successfully implemented upgrades such as magnetic-shielding that have revolutionized their capabilities. Agencies, companies, and academics worldwide remain highly interested in advancing Hall thruster technology for more powerful, efficient, and resilient space propulsion systems.

1.3 Motivation

The general motivation for this work was the optimization of the combined anode/gas distributor subsystem of the Adaptive-field Central-cathode Magnetically-shielded Electric (ACME) Hall thruster. The primary research pursuit of the ACME thruster is to characterize the influence of magnetic field topology on performance. This focus prioritized the design and optimization of some subsystems over others, and the anode was one aspect that was designed quickly and simply. The design directed propellant gas throughout the Hall thruster discharge channel sufficiently such that the thruster could operate properly, however the distribution of the propellant gas throughout the channel was suspected to be significantly non-uniform in the azimuth. Furthermore, the anode injected propellant axially into the discharge channel, which analytical theory and empirical evidence suggest increases the ionization mean free path, hence decreasing the mass utilization and total thruster efficiencies [13] [29]. Therefore, novel anode geometries that addressed azimuthal uniformity and axial velocity presented a pathway toward improved performance of the ACME thruster.

Relatively recent innovations in metal additive manufacturing have enabled the designing and production of parts with complex internal geometry to be possible and straightforward, particularly due to commercial operations offering affordable manufacturing services. However, there is sparse use of 3D-printed anodes in Hall thruster literature, so implementing them in ACME would inform the feasibility of the practice.

Thus, 3D-printing research-based anode designs for the next iteration of the ACME anode was a compelling project in the optimization of the thruster. Quantifying the azimuthal uniformity as a function of axial position in the thruster would inform the importance and effectiveness of anode design strategies.

1.4 Thesis Structure

The relevant physics of electromagnetism for understanding this work is presented in Chapter 2. Chapter 3 discusses the theory behind Hall thruster anode design and the novel

designs investigated for this thesis. The pressure diagnostic used to characterize propellant flow uniformity is described in Chapter 4, and the entire experimental apparatus is discussed in Chapter 5. Results are presented in Chapter 6. Comparisons to prior research and reflections on this work are made in Chapter 7.

Chapter 2

BACKGROUND

There are many excellent resources that detail in depth the breadth of EP technologies and the physics behind them. Here, I will describe only the essential aspects of EP physics necessary to follow this work, and I refer the reader to texts by Goebel et al. [13], Goldston et al., [14], and Jahn [20] for further reading. The following descriptions of electromagnetism and Hall thruster fundamentals are in essence a reproduction from sections of these texts.

2.1 Single Particle Motion

Two physical processes are critical for understanding the basic operating principles of Hall thrusters: cyclotron motion and the $\mathbf{E}\times\mathbf{B}$ drift velocity. Both can be derived by beginning with the Lorentz force equation that governs the motion of a charged particle with mass m, velocity $\mathbf{v}$, and charge q in the presence of a magnetic field $\mathbf{B}$ and an electric field $\mathbf{E}$:

$$\mathbf{F} = m\frac{d\mathbf{v}}{dt} = q(\mathbf{E} + \mathbf{v} \times \mathbf{B}). \tag{2.1}$$

First, consider the case that there is no electric field and that the charged particle is moving perpendicular to the magnetic field. Equation 2.1 becomes

$$\mathbf{F} = q(\mathbf{v} \times \mathbf{B}) = q\mathbf{v}_\perp \times \mathbf{B}. \tag{2.2}$$

The particle experiences a force that is both perpendicular to its velocity vector and the magnetic field, resulting in circular motion around an axis that is parallel to the magnetic field vector. This orbital-motion-inducing force is equivalent to a centripetal force, allowing for the relationship

$$\mathbf{F}_c = q\mathbf{v}_\perp \times \mathbf{B} = qv_\perp B = \frac{mv_\perp^2}{r}, \tag{2.3}$$

where r is the radius of circular/gyro motion. Solving for r yields

$$r = r_L = \frac{mv_\perp}{qB}, \tag{2.4}$$

which is known as the cyclotron or Larmor radius. The value $\frac{|q|B}{m}$ is defined as the cyclotron frequency, ω_c, which is the rate at which the particle completes orbits around a magnetic field line. The Larmor radius is therefore also given as

$$r_L = \frac{v_\perp}{\omega_c}. \tag{2.5}$$

This straightforward derivation reveals the fundamental principle of cyclotron motion: charged particles in the presence of a magnetic field will move cycloidally around field lines in orbits of radius r_L at a frequency of ω_c. Importantly, the magnitude of r_L increases proportionally with mass, meaning that for a quasi-neutral plasma of electrons and ions, the Larmor radius will be orders of magnitude larger for ions than electrons.

Next, consider again the Lorentz equation (2.1), but now in the case that the particle is in steady-state motion such that $\frac{d\mathbf{v}}{dt} = 0$. The equation becomes

$$\mathbf{E} = -\mathbf{v} \times \mathbf{B}. \tag{2.6}$$

Taking the cross product of this equation with the magnetic field gives

$$\mathbf{E} \times \mathbf{B} = (-\mathbf{v} \times \mathbf{B}) \times \mathbf{B} = \mathbf{v}B^2 - \mathbf{B}(\mathbf{B} \cdot \mathbf{v}), \tag{2.7}$$

but when $\mathbf{v}$ is perpendicular to $\mathbf{B}$ the final term is zero, thus

$$\mathbf{v} = \frac{\mathbf{E} \times \mathbf{B}}{B^2} \equiv \mathbf{v}_E \tag{2.8}$$

where $\mathbf{v}_E$ is defined as the $E \times B$ drift velocity, and is oriented in the direction perpendicular to both the electric and magnetic fields. This derivation reveals that electrons and ions in the presence of orthogonal magnetic and electric fields will drift in the mutually orthogonal direction: a phenomenon known as the Hall Effect, named after Edwin Hall. The current produced by charge carriers with velocity $\mathbf{v}_E$ is called the Hall current.

2.2 Hall Thruster Fundamentals

Hall thrusters consist of three primary components: an annular channel with a combined anode/gas distributor at its base; a magnetic circuit comprised of electromagnets and high-magnetic-permeability material that create a predominantly radial magnetic field across the channel; and a hollow-cathode that provides a source of electrons in the near-region external to the channel. The cathode can be mounted externally of the cylindrical channel or along the thruster center-line axis. There are two main kinds of Hall thrusters, stationary plasma thruster (SPT) and thruster with anode layer (TAL), the former of which will be the only one described in this work (henceforth referred to as simply 'Hall thruster'). Figure 2.1 shows a cross-section schematic of a typical xenon Hall thruster with an externally mounted cathode. The channel walls are made up of a dielectric materials with low secondary electron emission and sputtering yields such as boron nitride, borosil, or alumina [13]. An axial electric field is established between the biased anode near the back of the channel and electrons provided by the hollow cathode. This electric field ultimately accelerates ionized propellant to high velocities and generates thrust due to motion dictated by Equation 2.1. Electrons from the hollow cathode cannot traverse the channel directly to the anode axially due cyclotron motion imposed by the applied radial magnetic field. Assuming that the velocity perpendicular to the magnetic field $v_\perp$ of an electron entering the channel is equal to its thermal velocity of

$$v_{th} = \sqrt{\frac{8kT_e}{\pi m_e}}, \tag{2.9}$$

then the Larmor radius of the electron with temperature T_e is

$$r_{L,e} = \frac{v_{th}}{\omega_c} = \frac{m_e}{eB}\sqrt{\frac{8kT_e}{\pi m_e}} = \frac{1}{B}\sqrt{\frac{8m_eT_e}{\pi e}}, \tag{2.10}$$

where e is the elementary charge, m_e is electron mass, and k is the Boltzmann constant.

If the electron Larmor radius were equal in length to the plasma's characteristic length scale, L, then transport to the anode would be uninhibited. Thus, a fundamental relationship for a Hall thruster is that the electron Larmor radius is substantially less than L:

$$r_{L,e} << L, \tag{2.11}$$

Equation 2.10 shows that the Larmor radius decreases with magnetic field strength. Along with ensuring that the criterion in equation 2.11 is met, axial electron motion must also be limited by thorough magnetization of the electrons, meaning that they must on average complete many gyrations around a magnetic field line before colliding with an ion or

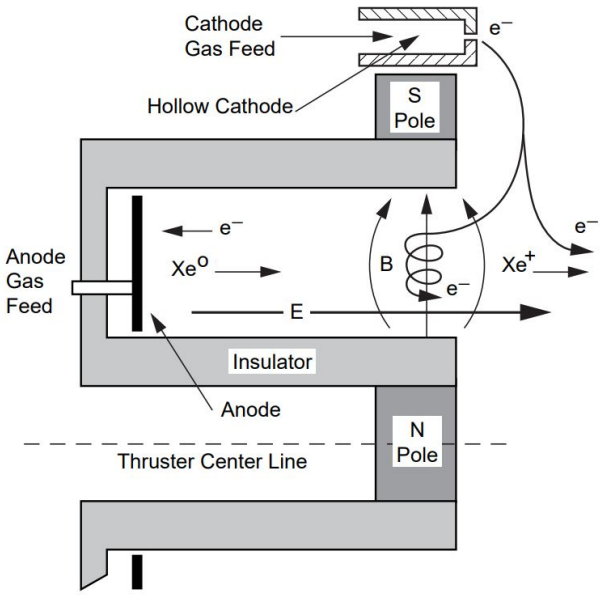

Figure 2.1: Cross-section schematic of a xenon Hall thruster with an externally mounted cathode, from [13].

neutral particle. These collisions are what ultimately cause electron diffusion to the anode despite begin 'bound' to magnetic field lines. The Hall parameter Ω_e is defined as the ratio of the cyclotron frequency to the total collision frequency ν, hence this magnetization condition is expressed as

$$\Omega_e^2 = \frac{\omega_c^2}{\nu^2} >> 1. \tag{2.12}$$

Similarly to equation 2.11, this condition is met by ensuring that the applied magnetic field is of sufficiently high magnitude. However, this magnitude is limited by the condition that in order to generate thrust, ions must be accelerated out of the channel by the applied electric field. As charged particles in a magnetic field, ions also undergo cyclotron motion, meaning too strong of a magnetic field would over-magnetize ions such that they do not escape the device with a high axial velocity. Presuming that the ion is singly charged, that its velocity is axial, and that its kinetic energy is equivalent to the electrostatic potential energy from the beam voltage V_b, an expression for ion velocity can be derived from energy balance

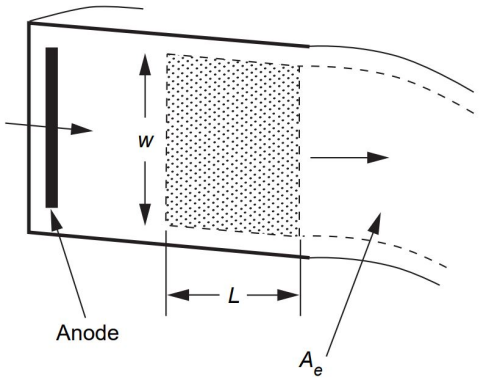

Figure 2.2: Cross-section schematic of a basic Hall thruster channel from [13].

$$\frac{mv^2}{2} = qV \tag{2.13}$$

$$\frac{m_i v_i^2}{2} = eV_b \tag{2.14}$$

$$v_i = \sqrt{\frac{2eV_b}{m_i}}. \tag{2.15}$$

The ion Larmor radius is therefore

$$r_{L,i} = \frac{v_i}{\omega_{c,i}} = \frac{m_i}{eB}\sqrt{\frac{2eV_b}{m_e}} = \frac{1}{B}\sqrt{\frac{2m_i V_b}{e}} \tag{2.16}$$

and must adhere to the condition that $r_{L,i} >> L.$ in order for ions to remain unmagnetized and their trajectories largely axial.

Where the transverse magnetic field is at a maximum, electrons undergo joule heating, increasing both electron temperature and the rate of ionization. Since the magnetization of electrons is greatest at this maximum, their mobility is limited and the axial electric field is also at a maximum. The region upstream of this dual peak is called the ionization region, and the region surrounding the electric field maximum is called the acceleration region. These regions comprise the characteristic scaling length/plasma thickness L which makes up most of the channel. The overlapping of the two regions results in dispersion in ion velocity and varying divergence angles of the ions exhausted from Hall thrusters [13].

Due to the presence of an axial electric field and a radial magnetic field, the electrons of the cathode potential plasma in the channel experience an $E \times B$ drift in the azimuthal direction as described by Equation 2.8, producing a Hall current. Since the electrons are mostly axially stagnant due to the magnetic field, force balance mandates that the electrostatic force on the electrons is equal to the Lorentz force. For the cylindrical Hall thruster geometry where the positive direction is that of accelerated propellant, this is described analytically as

$$\mathbf{F}_e = -2\pi \int\int qn_e \mathbf{E} r dr dz - 2\pi \int\int qn_e \mathbf{v}_e \times \mathbf{B} r dr dz = 0. \tag{2.17}$$

Assuming local quasi-neutrality and defining the Hall current density as $\mathbf{J}_{Hall} = -qn_e\mathbf{v}_e$, the axial force on the ions is equal to the Lorentz force on the electrons:

$$\mathbf{F}_i = 2\pi \int\int \mathbf{J}_{Hall} \times \mathbf{B} r dr dz = \mathbf{J}_{Hall} \times \mathbf{B}. \tag{2.18}$$

The Hall current force on the electrons is equal and opposite to the Hall current force on the magnets integrated into the thruster, and is also equal to the force on the ions given by Equation 2.18. Therefore, the thrust force on the Hall thruster is

$$\mathbf{T} = \mathbf{J}_{Hall} \times \mathbf{B} = -\mathbf{F}_i. \tag{2.19}$$

While every aspect of this description contains more involved physical processes, this is the general principle behind Hall thruster operation [13].

2.3 Ionization and Neutral Gas Dynamics

Neutral gas is injected at the base of the discharge channel through the anode, where it traverses axially towards the exit plane. The gas, most commonly xenon, krypton, or argon due to their large mass to ionization energy ratios, is ionized through coulomb collisions with energetic Hall current electrons in the region where the magnetic and electric fields are largely orthogonal. This ionization region is loosely defined, but is generally in the second half of the discharge channel near the channel exit, and even further downstream in magnetically-shielded Hall thrusters [23].

Consider the neutral gas traversing axially along the thruster center axis ($\hat{z}$) from the anode to the ionization region with velocity v_n and density n_n. Neutral velocity v_n is given by $v_n = \frac{dz}{dt}$ where z is the axial length from the anode. The flux of neutrals incident on the plasma is then

$$\Gamma_n = n_n v_n \tag{2.20}$$

If the quasi-neutral plasma has number density density $n = n_e = n_i$ and electron temperature T_e, then the density of the neutral population will decrease according to

$$\frac{dn_n}{dt} = -n_n n_e \langle \sigma_i v_e \rangle = \frac{d\Gamma_n}{d\Gamma_n} = -\frac{n_e \langle \sigma_i v_e \rangle}{v_n} dz \tag{2.21}$$

where $\langle \sigma_i v_e \rangle$ represents the ionization reaction rate coefficient for a Maxwellian electron population, which is a function of T_e. Substitution of Eq. 2.20 and the expression for v_n into Eq. 2.21 produces the relationship

$$\frac{d\Gamma_n}{\Gamma_n} = -\frac{n_e \langle \sigma_i v_e \rangle}{v_n} dz \tag{2.22}$$

The solution to this equation is given by

$$\Gamma_n(z) = \Gamma(0) e^{-(z n_e \langle \sigma_i v_e \rangle / v_n)} \tag{2.23}$$

$$= \Gamma(0) e^{-z/\lambda_i}, \tag{2.24}$$

where $\Gamma(0)$ is the neutral flux at the beginning of the ionization region and λ_i is the ionization mean free path. The ionization mean free path, or average length a neutral particle travels before an ionization reaction, is given by

$$\lambda_i = \frac{v_n}{n_e \langle \sigma_i v_e \rangle}. \tag{2.25}$$

Equation 2.25 demonstrates that the neutral velocity is directly proportional to the ionization of neutral propellant fed through the anode. As neutral gas atoms travel axially, the faster-moving electrons in the azimuthal Hall current inflict ionization reactions before neutrals pass the through the plasma thickness. Essentially, the axial neutral velocity dictates the dwell time in the region where ionization is highly probable. Furthermore, λ_i has an inverse relationship with the electron density since a denser population of electrons will increase the likelihood of an ionization collision as propellant passes through the Hall current plasma [13].

If the plasma has a thickness L, then the fraction of propellant that is ionized by the plasma before exiting the ionization region is

$$\frac{\Gamma_{exit}}{\Gamma_n} = 1 - e^{-\frac{L}{\lambda_i}}. \tag{2.26}$$

This flux ratio should be maximized such that as much propellant as possible is ionized to produce thrust according to Equation 2.19. Maximizing Eq. 2.26 requires that

$$\frac{\lambda_i}{L} << 1, \tag{2.27}$$

which is an important Hall thruster scaling law. For 90 percent of neutrals to be ionized, it is required that

$$\frac{L}{\lambda_i} > -\ln 0.1 \approx 3. \tag{2.28}$$

However, some fraction of ionized propellant collides with the channel walls or is re-neutralized in charge exchange reactions meaning that in practice a greater ratio would be required to achieve 90% ionization, hence the scaling law given in Equation 2.27.

Since thrust is equal to the electrostatic force imparted on the ions, it is immediately apparent that allowing some propellant ions to escape the thruster unionized represents a loss in efficiency as well as in the potential Δv of a spacecraft since the average exhaust velocity is reduced. In performance terms, the extent of ionization is described by the mass utilization efficiency

$$\eta_m = \frac{\dot{m}_i}{\dot{m}_p}. \tag{2.29}$$

where $\dot{m}_p$ is the total propellant mass flow rate and $\dot{m}_i$ is the ion mass flow rate. Mass utilization efficiency is a coefficient of the total efficiency and anode efficiency of a Hall thruster. Thus the neutral velocity, via its impact on the ionization mean free path, directly impacts Hall thruster performance.

2.4 Magnetic Shielding

A major limitation of SPT Hall thrusters is that high energy ion bombardment can cause erosion of the ceramic channel walls [13]. This occurs due to induced electric fields in the plasma that have a component parallel to the applied magnetic field and in the direction of the channel boundary. Erosion of the channel and other surfaces can eventually lead to device failure, which severely limits the deep-space use cases for Hall thrusters due to the immense burn time requirements of low thrust propulsion in interplanetary space. Moreover, erosion failure modes limit the economic viability and profitability of commercial satellites equipped with Hall thrusters for station-keeping, which is by far their most common use case. While solutions to the issue of channel erosion were suggested as far back as the 1960s, it was not until around 2010 that an effective magnetic shielding technique was developed

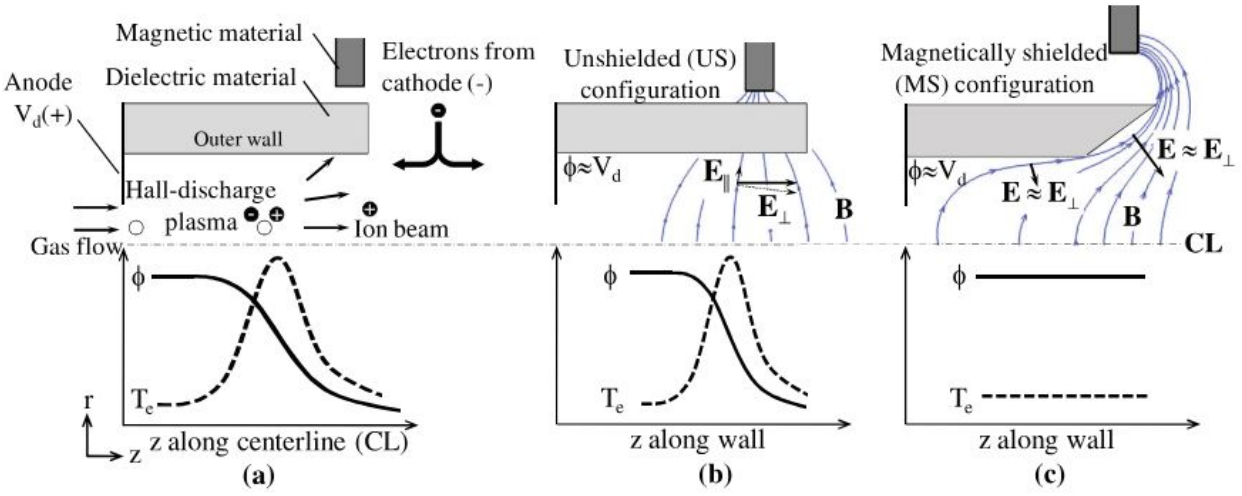

Figure 2.3: "Schematics of the upper half of the annular channel containing a Hall discharge (top) and typical profiles of and T_e (bottom) established during ion acceleration. (a) Basic features of the accelerator and typical profiles along the centerline. (b) **B** lines and profiles along the wall in an unshielded configuration. (c) **B** lines and profiles along the wall in a magnetically shielded configuration." From [25].

[13]. The shielding effect is produced by using an applied magnetic field topology with field lines that dip deeply into the channel, running parallel to the channel walls and near to the anode before becoming radial and rising back toward the exit plane. This topology achieves near-ideal equipotentialization of the lines of force near the channel walls, preserving the orthogonality of the **E** and **B** fields. Figure 2.3 from [25] depicts the important effects of magnetic shielding in a Hall thruster channel.

Magnetic shielding raises the potential propellant throughput of Hall thrusters by up to an order of magnitude, revolutionizing their viability commercially and as propulsion systems for deep space missions. NASA's Gateway, an orbital outpost on the moon, will incorporate the first flight model of a magnetically-shielded Hall thruster aboard its Power and Propulsion Element, launching in 2025 [13] [15].

2.5 The ACME Hall Thruster

The Adaptive-field Central-cathode Magnetically-shielded Electric (ACME) thruster is a research Hall thruster developed in University of Washington's Space Propulsion and Advanced Concepts Engineering (SPACE) Lab by PhD candidate Peter Thoreau and advisor Justin Little. As an undergraduate, I gained my first experience with electric propulsion by assisting Thoreau with the initial mechanical design and CAD modeling of the thruster. ACME is designed to be used as a testing platform primarily for studying the influence of magnetic field topology on magnetically-shielded Hall thruster performance and operation [32]. Figure 2.5 shows an image of the second iteration of ACME mounted on a nested inverted pendulum thrust stand, also developed by Thoreau.

Uniquely, the anode and inner magnetic pole of ACME are designed to be capable of translating axially relative to the outer magnetic pole. This adjustable channel geometry, depicted in Figure 2.4, allows for a vast amount of configurations of magnetic field topology, particularly when considering the electromagnet current strength is another variable that can be manipulated.

While the focus of the ACME thruster is to study the relationship between performance

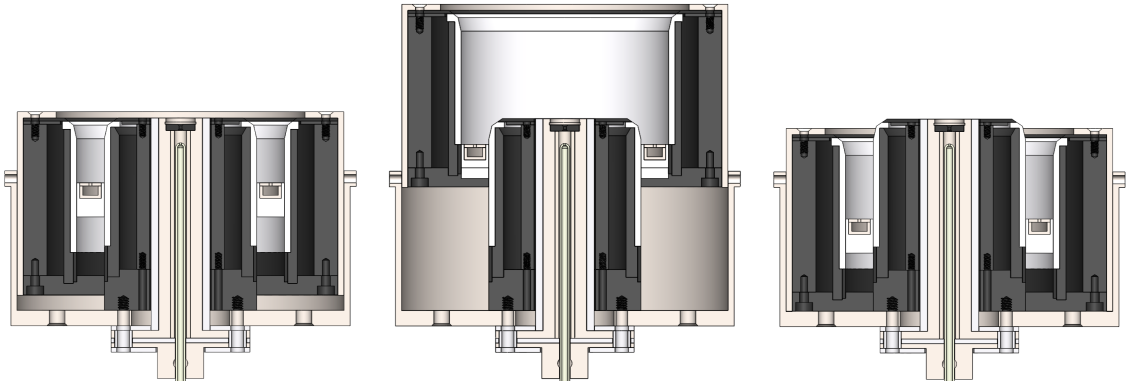

Figure 2.4: ACME is designed such that the relative positioning of the center pole, anode, and outer pole can vary substantially. Shown here is the full range of positioning. Left: the inner and outer pole at the 0 mm position, where ends of the inner and outer channel walls are flush. Center: the inner pole at the minimum position of -35mm. Right: Inner pole at maximum position of +5mm [32].

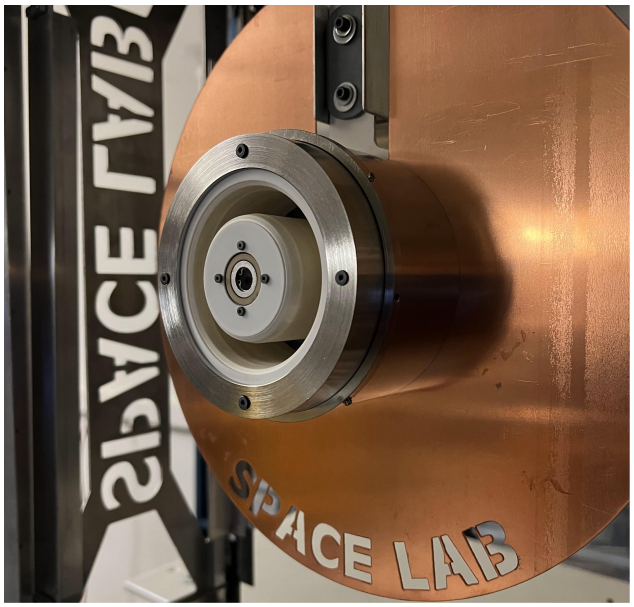

Figure 2.5: ACME mounted on the inverted pendulum thrust stand in the SPACE Lab [32].

and magnetic field topology, the thruster has become the SPACE Lab in-house test bed for numerous other Hall thruster and plasma science experiments. One area of interest for the ACME thruster was the effect that the propellant gas injection scheme through the anode had on mass and current utilization efficiency and performance. This topic and the desire to optimize the ACME anode subsystem inspired the experiment and findings presented in the following chapters.

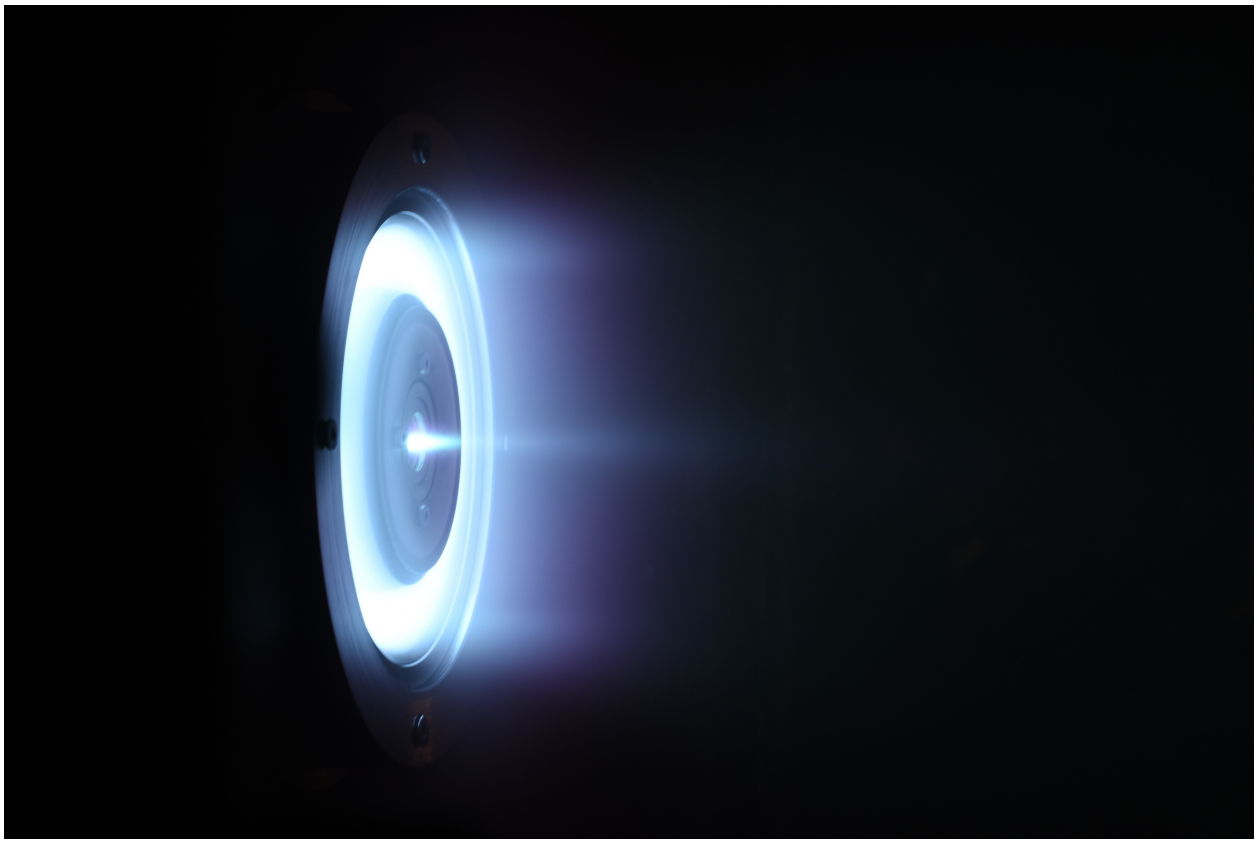

Figure 2.6: ACME Hall Thruster operating on xenon [32].

Chapter 3
ANODE DESIGN

In this chapter I present the theory motivating my experiment and the approaches taken to study the effect of anode geometry on the azimuthal uniformity of propellant gas.

3.1 Neutral Gas Azimuthal Uniformity and Residence Time

As discussed in Chapter 2, a fundamental aspect of Hall thruster operation is that electrons are inhibited from traveling from cathode to anode due to the applied magnetic field. While electrons are magnetized to field lines, they diffuse across magnetic field lines to the anode through a random walk process driven by collisions with neutrals [29]. Increasing the ionization mean free path would therefore limit this diffusion, and Equation 2.25 shows that this can be accomplished through decreasing electron density. A lower Larmor radius, attainable through increased magnetic field strength, would also decrease cross-field diffusion since the electrons would generally orbit further generally from the anode.

Near the anode, electrons are still magnetized despite the relatively weak magnetic field [29]. Since this region is where propellant gas is injected, the neutral density is naturally higher than downstream since little ionization has occurred. The relatively greater neutral density and presence of magnetized electrons results in heightened collisionality and thus mobility of electrons in the region near the anode.

Hofer found experimentally that an azimuthal uniformity in neutral density incurs a local increase in electron transport to the anode [17]. A manufacturing defect caused a single azimuthal location to have an augmented neutral density that was causally responsible for decreased thruster efficiency, plume symmetry, and stability. If only every mistake could lead to such an impactful discovery! In his 2004 PhD thesis, Hofer concludes that efficient

operation is dependent on the azimuthal uniformity of neutral flow through the anode. Conversano et al. found that asymmetry in neutral density also leads to a non-axial thrust vector [9].

The mechanism for this decreased efficiency is eloquently described in [29]: while most ionization occurs in the ionization region near the magnetic field maximum, some amount of ionization is occurring at all axial locations. Non-uniformities near the anode therefore produce a non-uniform plasma upstream of the ionization region. Electrons produced from ionization in this non-uniform plasma drift azimuthally due to the crossed electric and magnetic fields (Eq. 2.8), while the resulting ions remain unmagnetized since $r_{L,i} >> L$. The azimuthal non-uniformity of ionization produces ion density gradients that results in azimuthal electric fields. This then induces an axial $\mathbf{E}\times\mathbf{B}$ drift velocity for some electrons in the regions of ion density gradients that is oriented toward the anode. This increased electron current to the anode results in a lower average number of ionization collisions per electron, and causes a direct loss in thrust efficiency [13].

This description is supported analytically by Baranov [4], who showed that even a $\sim 10\%$ azimuthal discrepancy in density can cause substantial azimuthal ion currents and azimuthal electric fields that can even exceed the intensity of the axial electric field.

To demonstrate that increased electron current to the anode decreases efficiency, first consider that if the ion current to the cathode is small, the discharge current is approximated as the electron current to the anode

$$I_d \approx I_{ea}. \tag{3.1}$$

The current utilization efficiency of a Hall thruster is simply

$$\eta_b = \frac{I_b}{I_d} \tag{3.2}$$

where I_b is the current of the ion beam of particles escaping the thruster. If I_b remains constant since the rate of ionization and acceleration is unchanged, but azimuthal non-

uniformity results in increased I_{ea}, it is clear from Equation 3.2 that the current utilization efficiency will decrease. As current utilization efficiency is always the lowest of the efficiency terms that make up the total efficiency [13], any reduction is particularly harmful to overall efficiency.

3.2 Gas Injection Schemes

Among the methods to alter the neutral gas dynamics of a Hall thruster channel, manipulating the gas injection scheme is the easiest and most practical [28] [29]. Anode geometry can manipulate both the axial velocity and the azimuthal uniformity of the neutral gas, and therefore has a direct impact on thruster performance due to the relationships discussed.

Since the neutral velocity is affected by heating from the anode and the channel walls [18], the general injection direction affects neutral velocity substantially. Four primary methods of injection exist: axial toward the rear of the channel, axial toward the channel exit, radial towards the channel centerline, and radial towards the channel walls. In a study comparing axial injection, 'reverse' injection toward the rear of the channel was suspected to increase neutral temperature and was found to increase plume divergence, with little effect on efficiency [21]. For the ACME thruster specifically, reverse injection was not viable due to the nature of its construction. In order to modulate the channel geometry by changing the relative position of the inner and outer poles, the discharge channel is two pieces separated by a small gap at the base of the channel. While quite small ($\sim$ 0.2 mm), the gap had to be large enough to account for non-destructive thermal expansion. This gap leaves a path for propellant to stream behind the thruster, where it is wasted and potentially hazardous to operation of the laboratory thruster.

Among other designs, the state-of-the-art Magnetically Shielded Miniature (MaSMi-DM) and Advanced Electric Propulsion System (AEPS) Hall thrusters feature radial injection toward the channel walls, which was found to reduce axial velocity and improve ionization/mass utilization efficiency [6] [8] [24]. The positive results from these designs inspired the incorporation of radial injection into the two novel designs that sought to improve upon the original

ACME anode.

To increase azimuthal uniformity of neutrals, many different variations of baffles or internal distribution have been employed for different designs [24] [9] [29] . One interesting approach to producing a highly uniform azimuthal neutral pressure profile is forcing gas through a porous metal to inject the propellant into the channel [12].

Due to the suspected non-uniform propellant flow through the ACME anode and the relative simplicity of measuring density compared to velocity, the effect of anode geometry on azimuthal uniformity of neutral density was the focus of this research. Three anodes of different geometries were manufactured to study the neutral density profile differences between them and the original ACME anode. The primary intent of this research was to study how azimuthal uniformity evolved axially through the ACME channel for the different anode geometries.

Figures 3.3 - 3.10 are images and cross-sections of models of the four anodes studied, one of which is the original ACME anode (A1).

With research goals focused on other aspects of Hall thruster operation, the ACME anode was designed without optimization and manufacturing simplicity was prioritized. The main body of the anode is a stainless steel hollow toroid with a rectangular cross-section. Traditional manufacturing techniques were used in the construction of this hollow toroid, so it was necessarily comprised of two pieces brazed together: a U-shaped cross-section base and a flat annular face. At the center-radial position of the base piece (channel centerline), two 1.5 mm inlet holes are welded to stainless steel tubing that is routed straight through the main body of the thruster to where it is coupled to flexible propellant feed lines. On the face, twenty 1 mm outlet holes are drilled roughly along the centerline in a circular pattern.

Without internal baffles and with injection orifices spaced by $\sim 18^{\circ}$, the gas distribution was presumed to be substantially non-uniform. This was verified through photography of the ACME thruster during operation that showed increased luminescence in the regions near the gas inlet locations. By adjusting the color and exposure of the imagery, it was even possible to discern peaks of brightness that align nearly perfectly with the positions of individual

outlet orifices, as they are azimuthally offset by 18° (360°/20 orifices). Figure 3.1 depicts two photographs of the ACME thruster during operation, one unedited and the other with color adjustments. Note that these adjustments were made uniformly to the entire image, meaning the patterns illuminated are legitimate structures in the light data.

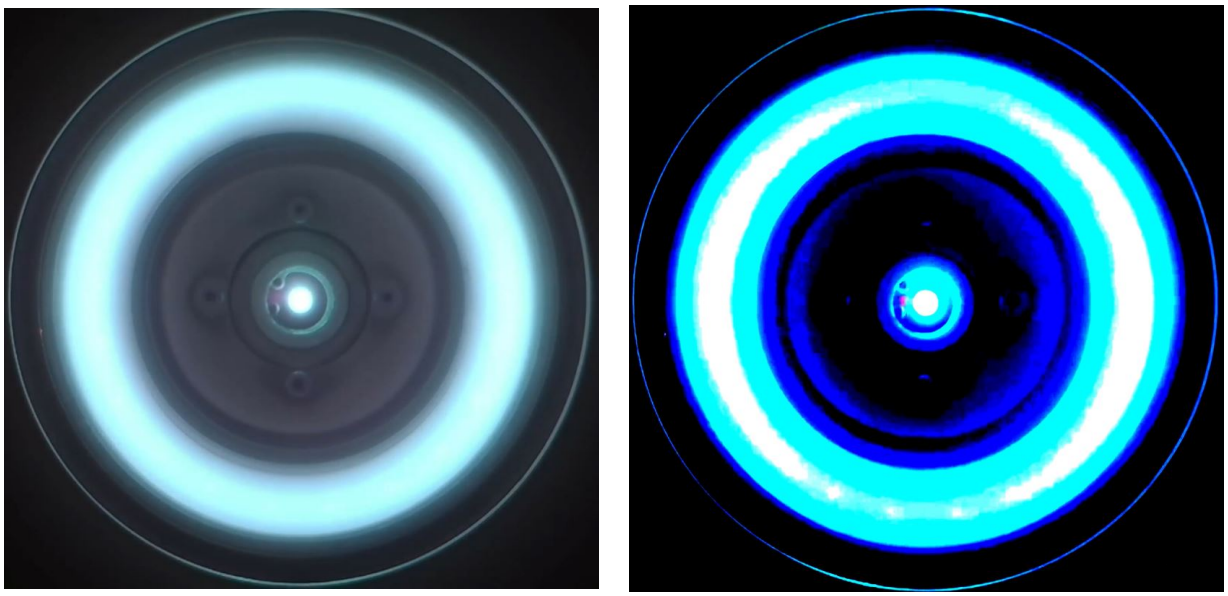

Figure 3.1: Comparison of a non-edited and edited photograph of the ACME thruster during operation. Left: unedited image. Right: same image as the left but with the brightness, contrast, and saturation altered, revealing distinctly the non-uniformities in the plasma density as indicated by the light intensity. The long white arcs are centered at the azimuthal locations of the gas inlet tubes, indicating the A1 anode did not thoroughly distribute the propellant. Individual bright spots seen in the lower portion of the image are due to local high densities associated with individual exit orifices, as they are separated by $\sim 18°$.

Additional confirmation of non-uniform neutral flow was visually confirmed in observing erosion on ACME insulation, where increased net erosion occurred in azimuthal regions nearer to the propellant feed inlet tubing, shown in Figure 3.2.

Furthermore, axial gas injection was suspected to be limiting the mass utilization effi-

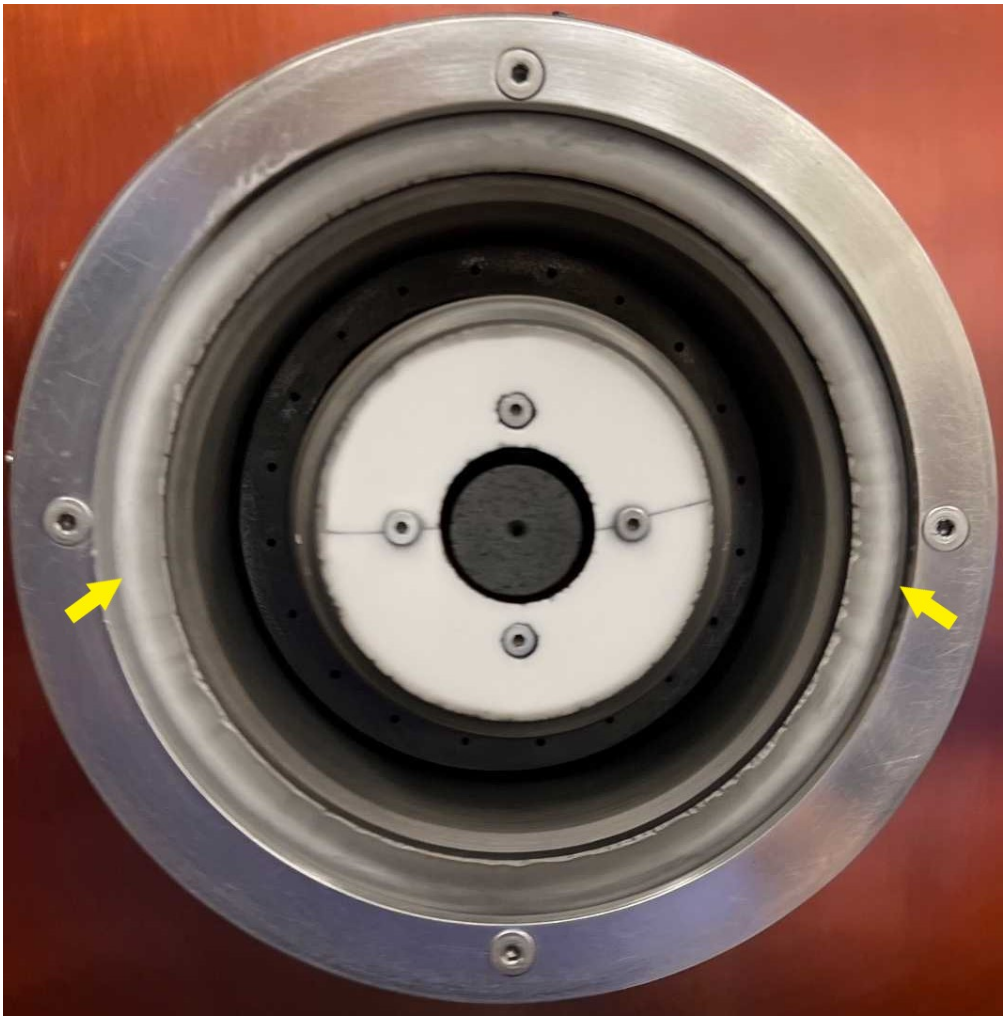

Figure 3.2: Non-Uniform erosion visible on the ACME Hall thruster. The areas of white on the outer ceramic annulus (alumina insulator) indicate net erosion, while the blackened areas are those with net deposition of carbon backsputtered from the vacuum chamber. The white eroded areas are predominantly seen on the lateral sides of the thruster (indicated with yellow arrows) near the azimuthal locations of the propellant feedthrough tubes. Note that the 'chips' in the insulator are artifacts from manufacturing, not plasma erosion.

ciency since the axial component of the neutral velocity directly impacts the ionization mean free path (Equation 2.25). A1 is shorter than the other anodes at 5 mm long in $\hat{z}$ rather

than 8 mm. The additional length was included to allow for more complex internal geometry while maintaining a size that is viable for operation in the ACME thruster.

The design shown in Figures 3.4 and 3.6 was labeled A2 and served as a benchmark case of severe non-uniformity in the azimuthal density profile. This prototype anode was printed out of polylactic acid (PLA) on a fused deposition modeling (FDM) printer in the SPACE Lab. The internal chamber is a pentagonal toriod with a single 4 mm outlet orifice located 90° offset circumferentially from the inlet orifices. The pentagonal cross-section was chosen as it mitigates the need for supports in the FDM printing of cavities.

Figures 3.7 and 3.9 depict the third design tested, A3. It features four chambers that are connected by an increasing number of equally spaced orifices. Gas is eventually injected from the fourth chamber out of 48 slots that are oriented in the azimuthal direction with a minor axial component. Inspiration for this injection scheme is from the findings presented by Xia et al., who found that rotational gas injection improved ionization efficiency, anode efficiency, thrust, and reduced the plume divergence angle [24] [33]. The complex geometry of this anode made of 316L stainless steel created with direct metal laser sintering (DMLS) 3D-printing conducted by Protolabs, a commercial manufacturer.

The fourth anode, A4, is shown in Figures 3.8 and 3.10. Two models of this design were 3D-printed by Protolabs, one of 316L stainless steel and the other of Nylon. Gas travels from the two inlet holes at the anode base to the middle of three lower volumes in the channel. Then, it is forced through 8 equally spaced openings at four azimuthal locations into the two adjacent volumes. The number of openings is doubled twice again before the path of the gas reaches the rear face of the channel-facing surface of the anode. Finally, gas is injected radially outward toward the channel walls from 128 square orifices at 64 azimuthal locations. The goal of the baffles in these anodes is to inject gas as azimuthally-uniform as possible by dividing gas flow from the two inlet tubes through consecutively more channels. Ideally, the exiting flow would come from one continuous outlet such as in the design proposed by [27]. However, a continuous outlet only injects gas with high uniformity if it is safe to assume that gas has fully mixed through the path of the final baffle. For instance, if the 20 orifices in A1

Figure 3.3: The original ACME anode (A1).

Figure 3.4: A2.

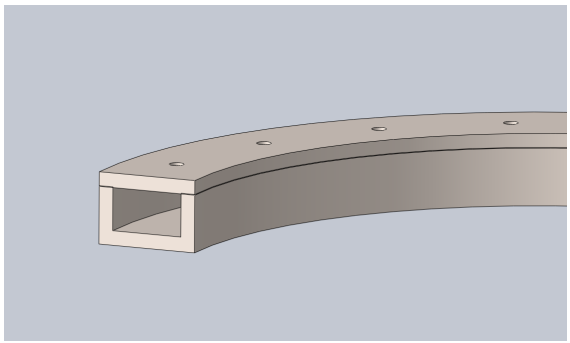

Figure 3.5: A1 cross-section.

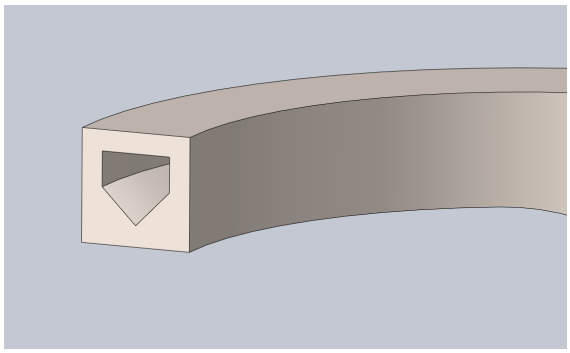

Figure 3.6: A2 cross-section.

were replaced with a continuous annular opening of the same width as an orifice diameter, the flow would not be azimuthally uniform since insufficient density homogenization has occurred from inlet to outlet. Another reason that many exit orifices were chosen over a continuous outlet is that the dividers between the orifices serve as structural supports for

channel facing surface. Conversano et al. [9] mentions that extending the channel facing surface radially a small amount beyond the orifice opening would prevent back-sputtered carbon (from vacuum testing) from eventually clogging some orifices. This approach was not adopted for A4 due to the aforementioned intention to mitigate reverse injection.

The test article for A4 was a 3D printed nylon version, made via multi jet fusion (MJF). The metal version was being actively used in ACME testing and was unavailable for the duration of this experiment. Indeed, each tested anode was manufactured differently, and therefore this research operates under the assumption that the material and manufacturing process play a negligible role in the gas distribution functioning of Hall thruster anodes. By extension, it is assumed that any differences in gas conductance or porosity of the tested materials do not largely effect the results of the experiment. Part of the validity of these assumptions hinges on the stated quality and tolerancing of the 3D printing models from Protolabs. The minimum feature size of DMLS stainless steel is claimed to be 0.381 mm and a layer thickness of 30 microns, while the minimum feature size and layer thickness of MJF Nylon is 0.5 mm and 80 micron, respectively [1] [2]. No feature or dimension on either A3 nor A4 is greater than 0.5mm, so theoretically the geometry of the anodes should be generally independent of material. Realistically, gas conductance and feature tolerance will have some material dependence. Figures 3.11 and 3.12 are close-up images showing the texture of the printed stainless steel and nylon, respectively.

For the metal-printed anodes, steel gas feed tubes were welded to the main anode body (Figure 3.13). The Nylon and PLA anode prototypes were affixed to tubing with two-part epoxy resin.

Figure 3.7: A3.

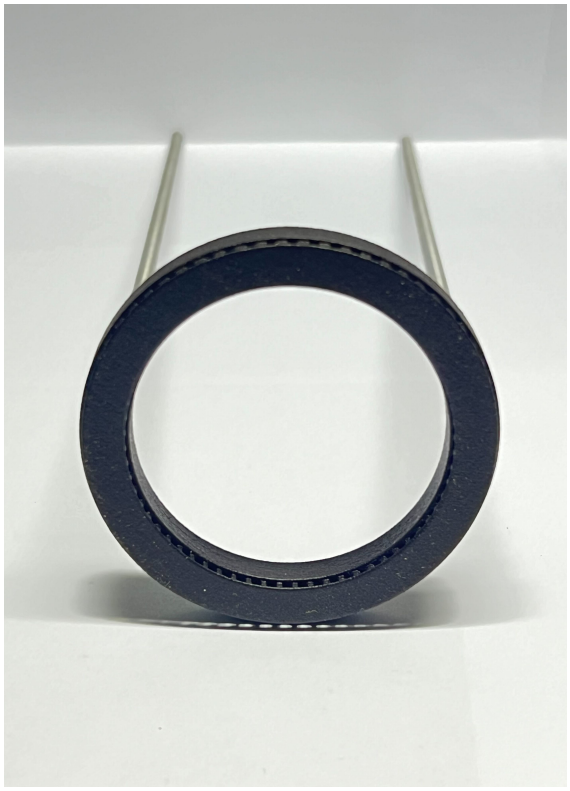

Figure 3.8: A4.

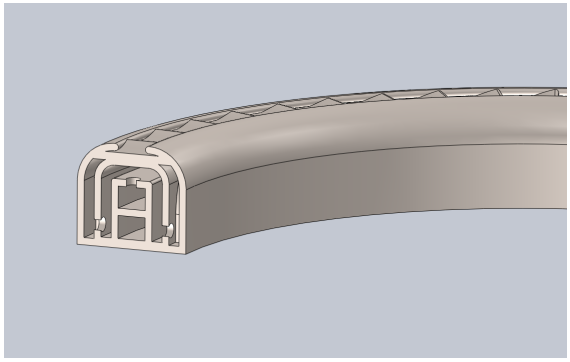

Figure 3.9: A3 cross-section.

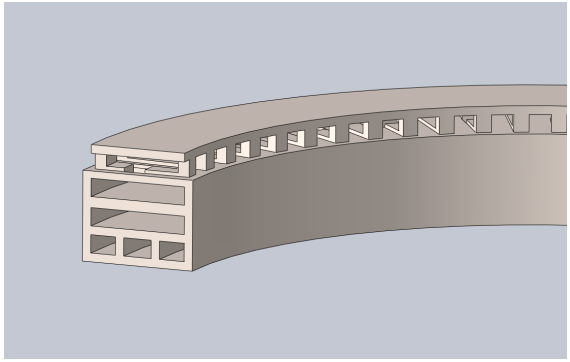

Figure 3.10: A4 cross-section.

Figure 3.11: Detail of the DMLS steel on A3

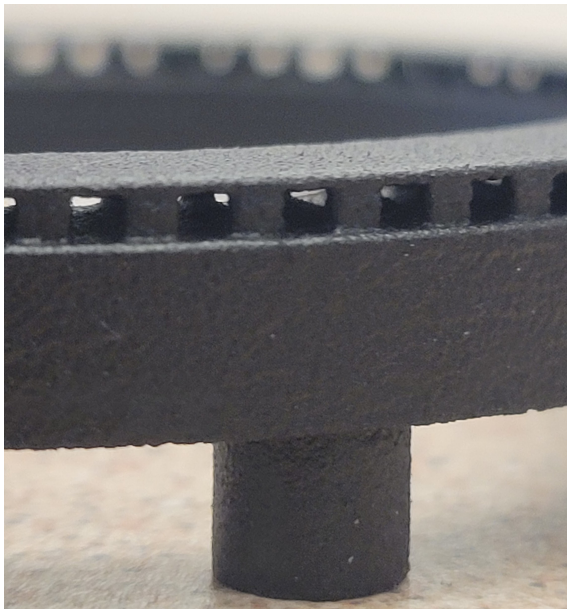

Figure 3.12: Detail of the MJF nylon on A4

Anode	**Material**	**Manufacturing**	**Gas Injection**	**Orifice θ Positions**
A1	S. Steel	Traditional	Positive Axial	20
A2	PLA	FDM Printed	Positive Axial	1
A3	S. Steel	DMLS Printed	+ Axial & Azimuthal	48
A4	Nylon	MJF Printed	Radial Toward Wall	64

Table 3.1: Key characteristics of the four tested anode designs.

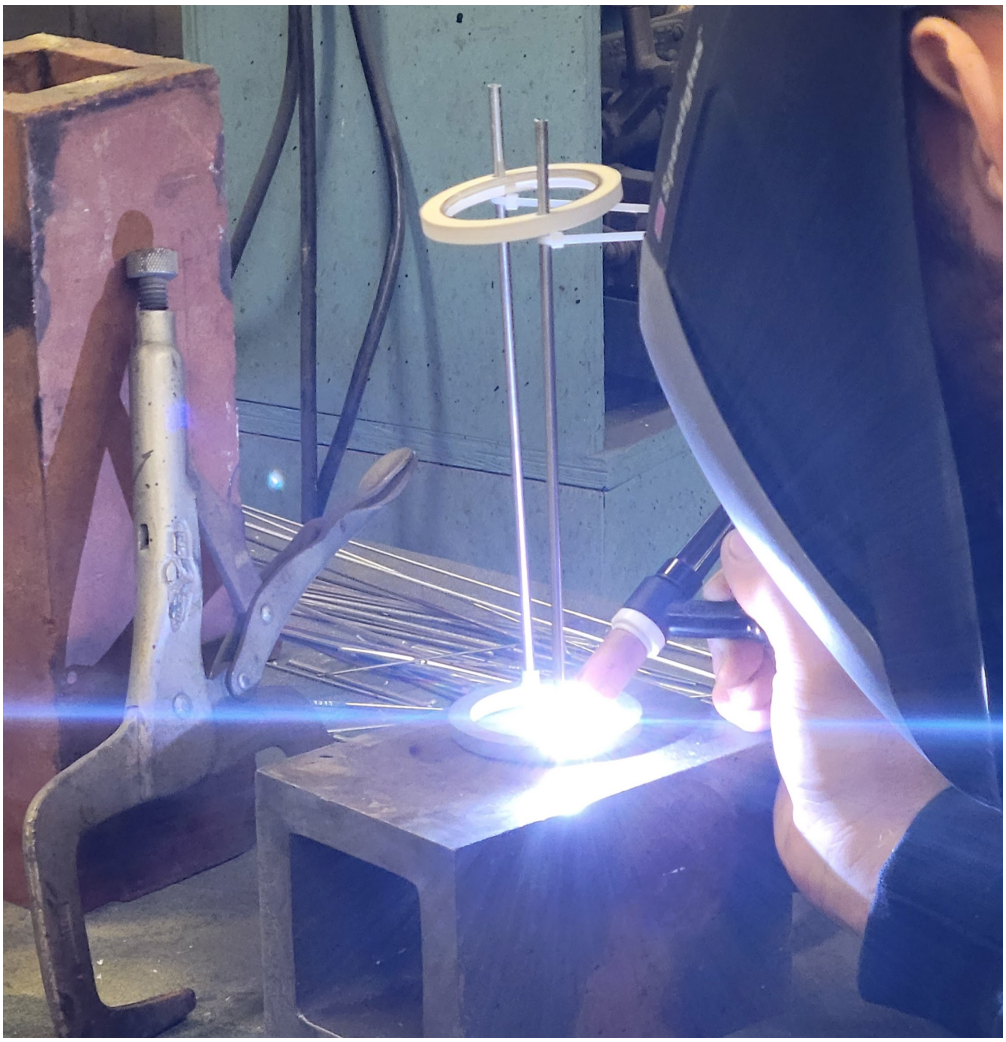

Figure 3.13: Welding steel gas tubes to the rear inlets of the 3D- printed anodes. The ACME ceramic anode insulator is used as a jig for correctly positioning the tubing. This welding was the only additional manufacturing step conducted after receiving the printed anode bodies of A3 and A4.

Chapter 4
NEUTRAL PARTICLE DIAGNOSTICS

Both optical diagnostics and electrostatic probes have been used extensively to measure the neutral density in Hall thruster discharge channels [24] [29]. While optical diagnostics such as laser induced fluorescence are particularly powerful at determining some neutral characteristics, electrostatic probes are attractive for density measurements due to their ease of use, requiring comparatively little support equipment or setup. Most approaches to electrostatic probe measurement of neutral particles within Hall thrusters involve using an ion gauge with a modified inlet placed in the neutral flow, typically aligned axially in the channel center [8] [12]. Pitot tubes have been used as inlets and paired with pressure transducers such as ion gauges or Pirani gauges in some of the most rigorous research of neutral pressure through Hall thruster anode/gas distributors to date [28].

4.1 Fast Ionization Gauge

The diagnostic used for gas flow uniformity testing in this work was a Beam Dynamics Model FIG-1 Fast Ionization Gauge, consisting of the Model FC-1 Control Unit and the Model FH-1 Gauge Head. The gauge head, referenced henceforth as the "FIG," is essentially a small, nude Bayard-Alpert (hot-filament) ionization gauge with a rise time of less than 5 μs. Its operational pressure range is from 10^{-8} to 10^{-2} torr and outputs a signal from 0 to -10V. Important properties of the FIG can be found in Table 4.1.

A diagram of a typical Bayard-Alpert ionization gauge is shown in Figure 4.1. This type of pressure gauge operates by heating a cathode filament, typically made of tungsten, that emits electrons at a carefully controlled rate. These electrons are attracted to a positively charged wire grid electrode, accelerating toward it according to the set potential of the grid.

Rise time	Pressure Range	V_{grid}	$V_{collector}$	$I_{emission}$	$V_{filament}$	$I_{filament}$
< 5 μs	$10^{-8} - 10^{-2}$ torr	160 V	0 V	5 μA - 3mA	2 V	2 A

Table 4.1: Beam Dynamics Model FIG-1 Fast Ionization Gauge Characteristics [5]

Some electrons pass through the volume enclosed by the grid, colliding with and ionizing neutral gas molecules present in the vacuum. These positive ions travel to the collector wire located along the axis of the grid electrode that is biased to 0 V. The current to the central collector wire is directly proportional to the gas density and pressure within the vacuum system for pressures below $\sim 1 \times 10^{-3}$ to $\sim 1 \times 10^{-2}$ torr [26] [31].

The grid and filament wires of the FIG are made of 0.005" diameter tungsten, while the collector, electrodes, and gauge frame are made of stainless steel. The otherwise nude gauge, pictured in Figure 4.2, has an aluminum alloy housing that both stabilizes the collector wire and prevents damage to the sensitive components.

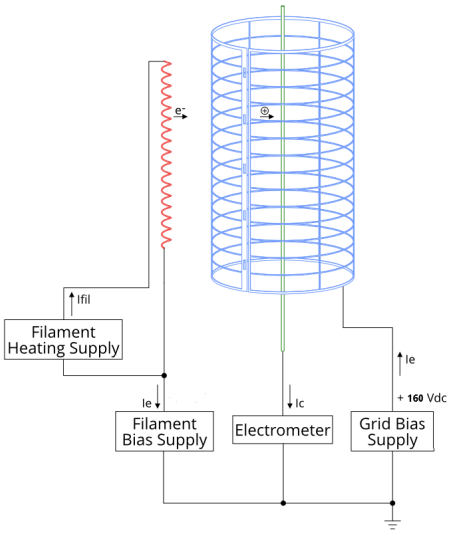

Figure 4.1: Schematic of a typical Bayard-Alpert Ionization Gauge [3].

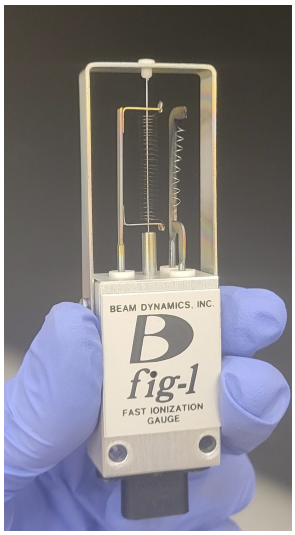

Figure 4.2: Beam Dynamics Inc. Model FH-1 Gauge Head.

For typical use of the FIG, it is mounted with two machine screws to any surface within a vacuum chamber, given that the surface can serve as a sufficient heat sink. Insufficient heat sinking causes thermal baseline drift of the output signal, and potentially damaging heat buildup if the temperature of the FIG body exceeds 70° C. The FIG accepts a cable that is routed to a vacuum feedthrough. On the external side of the feedthrough, a cable connects the feedthrough pins to the FIG controller. This controller supplies power to the FIG electrodes and electronics, and allows the user to set the filament emission current. The controller outputs a DC signal from 4 mV to -10 VDC via a BNC jack.

4.2 Modifications

The active area for beam or gas flow detection is the grid: a cylinder of approximate length and diameter of 25 mm and 3 mm, respectively. Therefore, the unmodified FIG has a spatial resolution of the cross section of the cylindrical grid: a 3mm x 25 mm rectangle [5]. To achieve a finer spatial resolution for the FIG pressure measurements, multiple modifications were made to the gauge. The aluminum mounting arm to which the FIG is nominally fastened was coupled with a slotted aluminum cylinder that could accept a tubular brass capsule. This brass capsule is sheathed over the FIG and cylinder, and features a narrow brass tube at its center. An exploded view of a CAD model for the modified FIG assembly is shown in Figure 4.3, and a photograph of the FIG assembly is shown in Figure 4.4. This capsule functionally reduced the spatial resolution of the FIG to that of the 0.066" inner diameter of the tube, allowing for local measurement of differences in pressure. While a smaller inner diameter would increase the spatial resolution of measurements, it also increases the settling time of the modified pressure gauge due to the decreased gas conductance to the gauge [11] [28]. Since continuous swept measurements were desired for this experiment, an inlet tube with too small of an inner diameter could substantially diminish the magnitude of deviations from the mean. The inner diameter of 0.066" was selected as a size that balanced resolution with measurement magnitude, and is within the range used for similar experiments [11] [28].

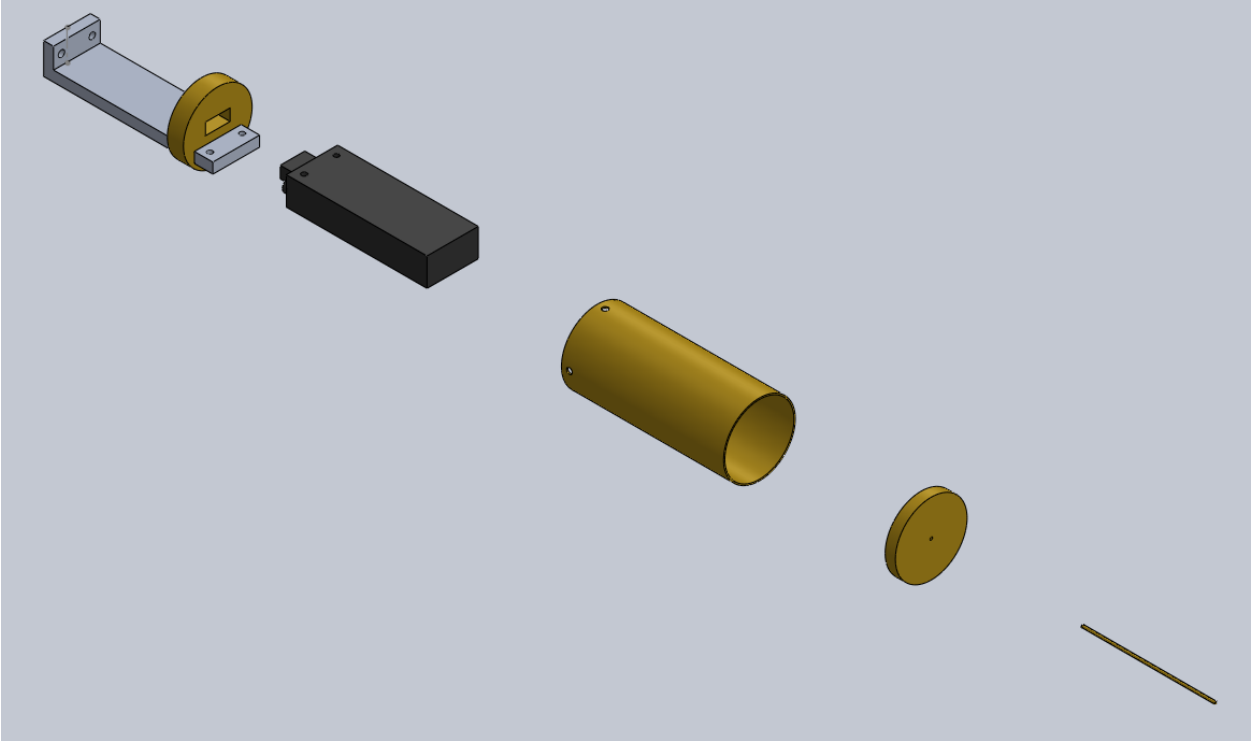

Figure 4.3: Exploded view of the modified FIG assembly CAD model. The black body represents the FIG.

4.3 Troubleshooting

While it is excellent at quickly and accurately measuring relative neutral gas density, the FIG proved to be a troublesome device. The manual dates to 2001, which could be considered young in comparison to other legacy laboratory equipment, however there is essentially no documentation online about the Beam Dynamics Fig-1 gauge head. Nor does there appear to be any readily for sale or resale, and Beam Dynamics has no contemporary information regarding the device [19]. Here, successes in troubleshooting and remarks on the usage of the FIG will be noted for the benefit of any future user, to be used in conjunction with the information in the manual.

Figure 4.4: The assembled modified FIG diagnostic. The FIG is sheathed inside the large brass with a pitot-end on the right and a sealed end with a small opening for the connector cable.

4.3.1 Grid and Collector Shorts

The space between grid electrodes and collector wire is ∼1 mm. Should the grid and collector wires contact each other, there will be a short and the LF357H (or NTE937 or equivalent) operational amplifier will be destroyed and in need of replacing. This happened frequently, as it is difficult to position the collector wire exactly axially through the holes in the electrodes, particularly when the FIG is being translated or rotated. The problem is evident when the signal from the FIG reads ∼ -15V on an oscilloscope and does not respond to changes in pressure. A test switch on the controller allows for the testing of the op-amp without vacuum by switching on the FIG without powering the filament. In this test mode, if the signal is ∼ -15V, the op-amp is broken.

Even when substantial care was taken to position the wire and electrodes correctly, movement of the FIG appeared to cause drifting of the relative positions of the grid and collector, and consequently causing contact and shorts. To address this issue, two short, small diameter alumina tubes were sheathed over the collector wire such that they made a dielectric barrier between the grid and collector electrodes at the locations where shorts were occurring. While this successfully addressed the shorting of the collector and grid and appeared to work at times, it is suspected to have caused the FIG to cease to function repeatably or reliably. Thus, the insulator modification was abandoned, as well as the original approach of rotating and translating the FIG the stationary anode assembly (Figure 5.4).

4.3.2 Filament Failure and Replacement

If the FIG filament does not glow, it is broken and can be replaced relatively easily. Eight turns of a 0.005" diameter tungsten rod must be tightly wound around a 0.063 in. diameter rod and spot-welded to the filament electrodes. The axial length of the coil must be short enough so that the filament is in tension when installed. The specific characteristics of the filament mentioned here appear to be essential for the proper functioning of the FIG. After one failure of the filament, a replacement filament was used that was shorter and had fewer coils than is specified in the manual due to a temporary lack of replacement filament wire. While the filament glowed and appeared to function properly for minutes after being turned on, after additional time the output signal from the controller was found to drift extremely and sporadically, blatantly not scaling proportionally with pressure. Narrowing down the cause of this erroneous behavior from the FIG took a substantial amount of time due to necessary vacuum pump-down cycling, but appeared to be resolved after ensuring that the filament met the near exact specifications in the manual.

4.4 Uniformity Acceptance Criteria

NASA and other researchers developing Hall thruster anodes with gas flow of high azimuthal uniformity have created standard criteria that designs must pass to be considered

acceptable. The criteria are specifically applied to testing procedures that generally follow the methods of the Anode Pressure Acceptance Test (APAT) conducted by Reid et al. [28], where an axially aligned pressure transducer/probe measures an azimuthal sweep at the anode centerline halfway between the anode face and channel exit plane. The first criterion, used for anodes of thrusters such as MaSMi-DM, H9, HERMeS, and more [9] [16] [10], is that the maximum pressure deviation from the mean must be less than or equal to 5%. Similarly, this criterion has been expressed as the peak-to-peak deviation from the mean not exceeding 10%, expressed in [16] as

$$\frac{\delta P_{max}}{\langle P \rangle} = \frac{P(\theta)_{max} - P(\theta)_{min}}{\langle P \rangle}. \tag{4.1}$$

The procedure and apparatus employed in this research is similar to that used in the referenced APAT, however the diagnostic and pitot assembly differs somewhat and more axial locations were measured. Since the APAT is applied at the $z = L/2$ axial location, it is sensible that the equivalent acceptance threshold values would be greater at locations upstream of $z = L/2$ and lower at locations downstream. While the standard acceptance criteria establish a binary yes/no decision of design acceptance, more stringent thresholds applied at locations upstream of $z = L/2$ would yield designs with better azimuthal uniformity, and thus thrusters with better performance due to the aforementioned processes of efficiency losses.

Chapter 5

EXPERIMENTAL FACILITY AND APPARATUS

This chapter describes the hardware systems used in the experiment in conjuction with the FIG pressure diagnostic. As the project advanced, substantial adaptations and changes to the apparatus were made as problems were encountered. Preliminary testing was conducted in three different vacuum chambers before troubleshooting succeeded and data were produced consistently and reliably. This section will only detail in depth the final testing apparatus.

5.1 Space Propulsion Experiments and Cryogenic Test EnviRonment (SPECTER)

All data presented were collected from testing conducted in the Space Propulsion Experiments and Cryogenic Test EnviRonment (SPECTER), a vacuum chamber in University of Washington's SPACE Lab. SPECTER was disassembled, refurbished and enhanced during the summer months of 2023, and is approximately 2.5 m long and 1.4 m in diameter. SPECTER is equipped with a Leybold D60A roughing pump, a Leybold WS250 roots blower, an Edwards XDS10 scroll pump, a Varian V-551 Navigator turbomolecular pump, and two custom cryosails that are designed around the Sumitomo CH-110LT cold head. The roughing pump and roots blower were used to expedite the pump-down process, but were shut off and isolated from the main chamber volume with a gate valve once the pressure was low enough for safe use of the turbopump. This isolation ensured that the oil-based roughing pump could not contaminate the chamber and turbopump in the event of an electrical or other failure. The cryogenic pumping capabilities of SPECTER were not necessary nor utilized for the base pressures required for testing of axial neutral gas profiles through different anode geometries. The interior walls of SPECTER are lined with reflective-white multi-layer

insulation to improve the performance of the cryosails and will be essential for planned thermal vacuum capabilities. The minimum background pressure attainable within SPECTER while operating solely on the scroll-pump-backed turbopmup was $\sim 1 \times 10^{-5}$ torr. Chamber pressure was monitored using both cold-cathode and thermocouple pressure gauges.

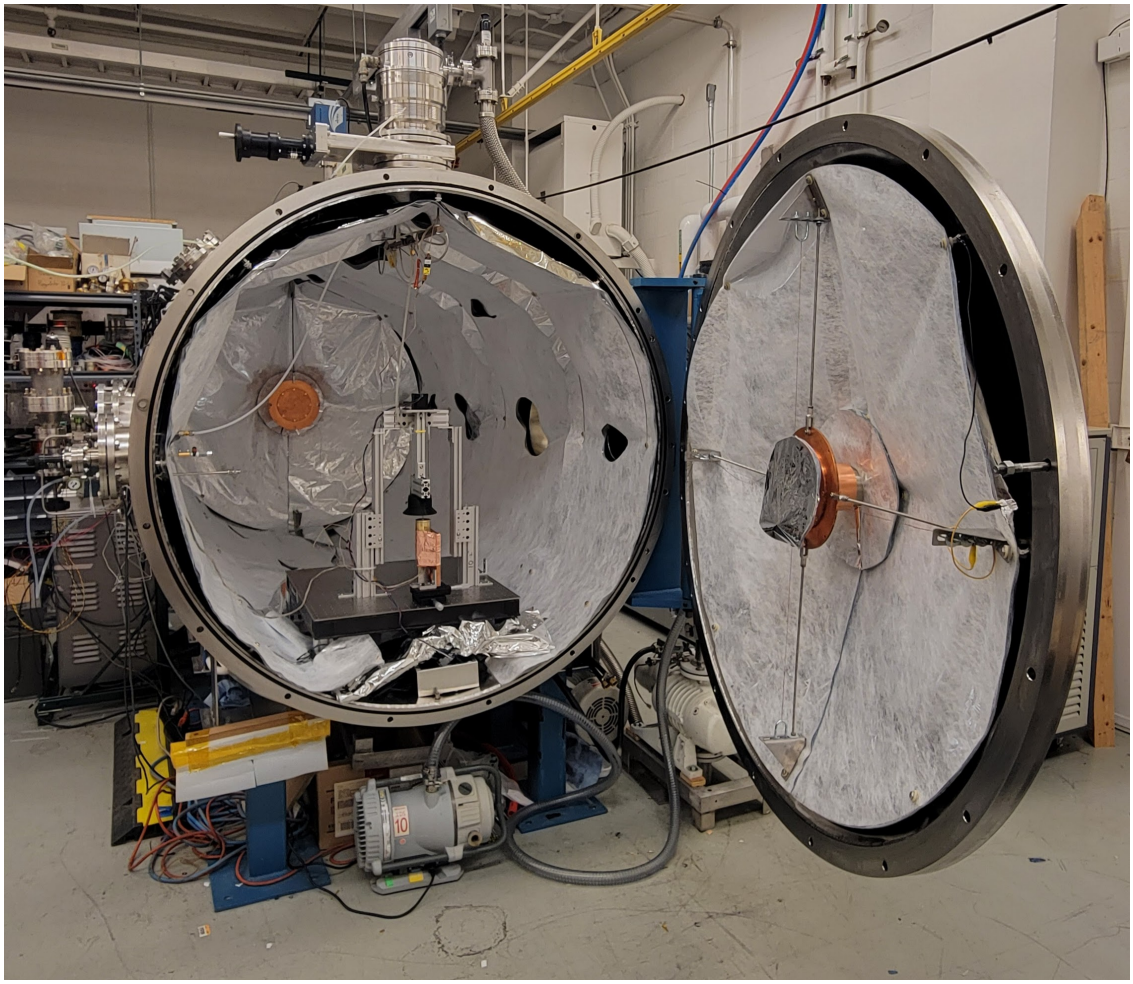

Figure 5.1: SPECTER, the vacuum chamber used for neutral flow testing, with the door open. The scroll and turbo pumps are above and below the vertical axis of the chamber, while the roughing pump and roots blower are seen to the right of the main chamber volume. The copper plates of the cryosails are visible at the center of the door and rear of the chamber. The testing apparatus atop an optics table is seen positioned at the center of the chamber.

To adequately simulate the neutral gas flow through a Hall thruster, the pressure must be low enough such that Knudsen number was in the free molecular flow regime. As the pressure range during testing was always between 1×10^{-3} and 1×10^{-2} torr, the Knudsen number corresponding to this range is greater than 10, and therefore within the required regime [11].

5.2 Apparatus

Figure 5.2 depicts a schematic of the entirety of the testing apparatus and vacuum chamber facility. The experiment consists of two main subsystems: the anode assembly and the diagnostic staging. The overall objective was to manipulate the relative position of a pressure sensing diagnostic and the anode/channel assembly to create relative pressure profiles for different anodes and testing parameters.

The modified FIG was used as the pressure diagnostic. To avoid deflection of either the anode or diagnostic assembly structures that could lead to erroneous relative positioning, the two subsystems were mounted such that their axes were aligned vertically with gravity. The subsystem center axes were aligned to be concentric to a tolerance of ± 1 mm through an iterative truing method.

The original approach to the setup was to fix the anode and replica thruster channel and use a combined rotation-translation stage that would move the FIG azimuthally and radially in the channel. Shown in Figure 5.4, this stage was manufactured and performed its intended function, but malfunctioning of the FIG was pervasive during this iteration of the apparatus. Insufficient heat sinking was thought to be a source of malfunctioning, and adding supplemental heat sinking was difficult in conjunction with use of the combined stage. Thus, the second implementation of the apparatus involved a better heat sunk, static FIG and a rotating anode assembly as shown in Fig. 5.5. This change did not solve the problems that were occurring with the FIG, indicating that some other source was responsible for them. Troubleshooting eventually yielded a reliable, operational FIG, and the second implementation was maintained to avoid introducing further issues with the FIG. Unfortunately,

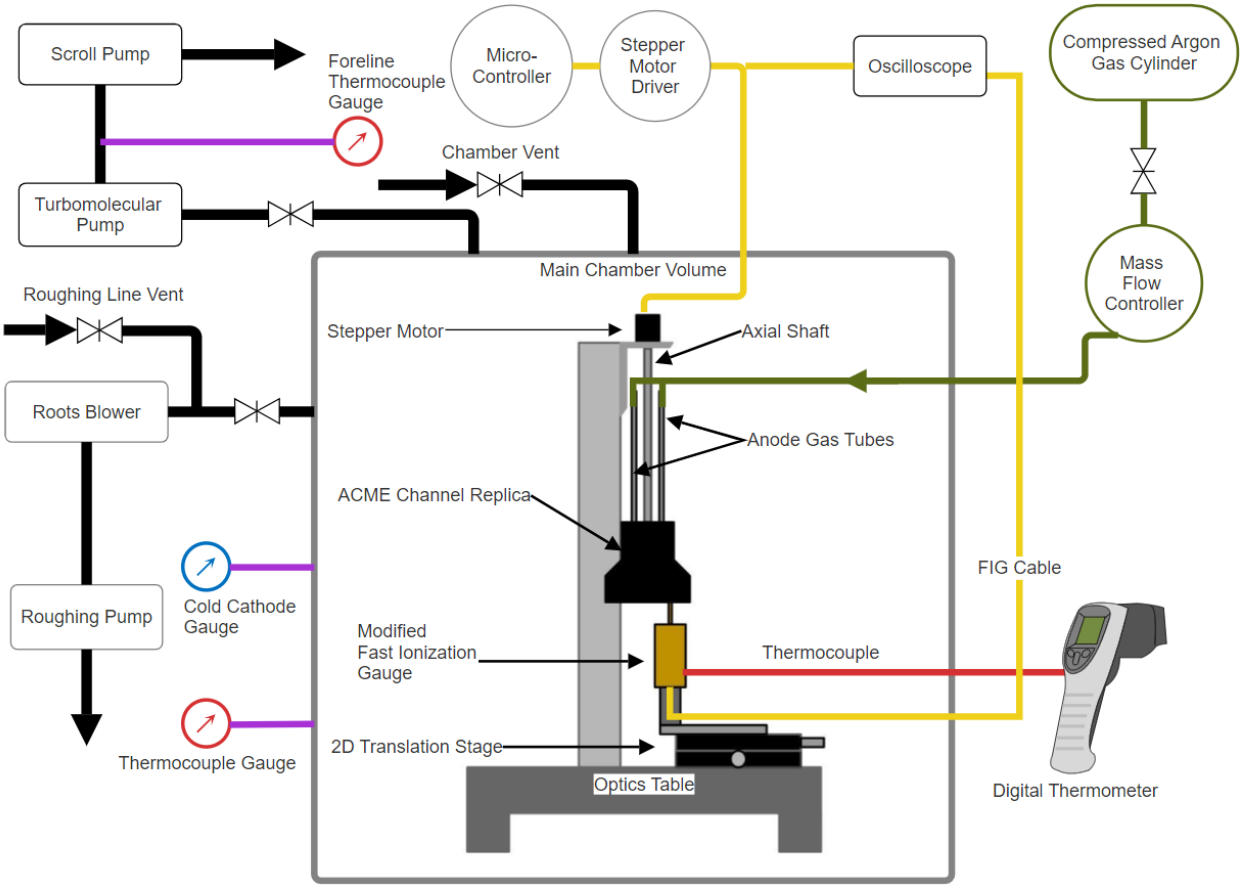

Figure 5.2: Schematic of the experimental apparatus.

the second testing approach forced the abandonment of data collection along different radial positions within the thruster channel. Instead, only the center of the channel was measured at various axial distances. Axial positions were set by sliding the rotational anode assembly along a vertical rail structure.

The FIG was mounted atop two stacked translation stages that allowed for positioning in the center of the channel to an accuracy of ± 0.1 mm in two dimensions. A large copper block was fastened to the translation stages held in contact with the external surface of the modified FIG to provide heat sinking. Additionally, copper tape was used to further compress the FIG into the copper block while also securing a type-K thermocouple to the

exterior of the FIG. The output signal from the FIG controller was passed through a 23 kHz low-pass filter to reduce environmental/electrical noise.

The anode assembly consisted of an anode body with two gas feed tubes embedded into a replica ACME Hall thruster channel that was 3D-printed out of PLA. Figure 5.3 shows an image of the replica ACME channel used for testing. Anodes were placed within a physical channel because measurements of gas flow through anodes alone has been shown to drastically underestimate pressures off of the anode centerline [28]. The ACME replica featured all pertinent geometric details of the annular ACME channel and was printed via FDM with 0.14 mm layer height and 100% infill to avoid out-gassing in vacuum. Mounting points were modeled into the back of replica so that it could be easily fastened and accurately positioned with laboratory structural equipment. The central axis of the axisymmetric channel was aligned to be coincident with the shaft of the Nema 16 stepper motor which was coupled to a larger connector shaft that the printed channel mounted to. A micro-controller and a DM320T stepper motor driver controlled the rotational actuation.

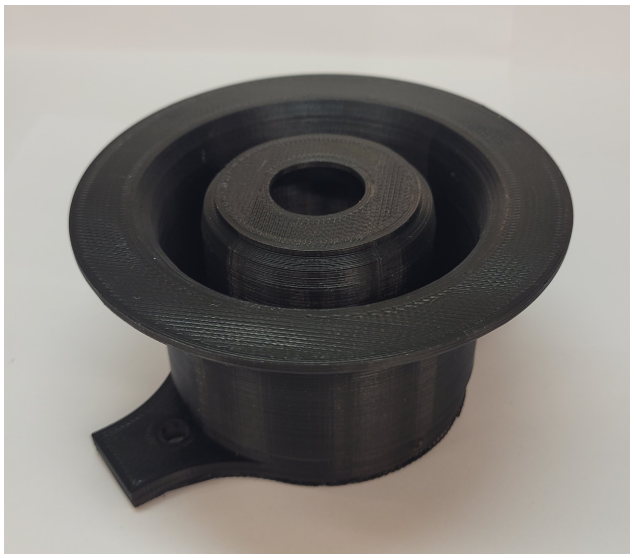

Figure 5.3: ACME thruster replica channel. The replica is 3D printed out of PLA and contains all geometric features of the channel components combined into a single body.

Each anode tested was positioned 26 ± 0.1 mm from the channel exit plane, as this is the nominal position of the ACME anode. Anodes were fixed into place with setscrews tapped through the exterior of the replica thruster that pressed into the gas feed tubes. Flexible gas tubing was routed from the anode tubing to an Alicat mass flow controller that was supplied by the SPACE lab gas distribution manifold.

5.3 Testing Procedure

Each test began with the positioning of the anode relative to the FIG. The anode axis was aligned to within ± 0.5 mm of the stepper motor shaft axis, and the FIG inlet tube was placed to within ± 0.5 mm of the channel centerline. After careful placement and alignment, SPECTER was pumped down until pressures from 1×10^{-5} to 5×10^{-5} torr were reached. Then, the FIG was switched on and allowed to warm up until its output signal, as read by the oscilloscope, became nearly constant on the scale of minutes. The FIG experienced predictable thermal drift that was linear on the time scale of the azimuthal sweep duration used for data collection (1.5 rpm), which could easily be corrected for relative comparisons. Just before flowing gas through the anode, pressure from the cold-cathode gauge, FIG temperature from the thermocouple, and the FIG output voltage were recorded. This voltage is the FIG 'null' signal for a current temperature and zero-flow base pressure. Due to variations in base pressure and FIG temperature that impacted the FIG reading, this null signal had to be accounted for when calculating relative pressure profiles. It was thought that the FIG thermocouple reading would need to be further accounted for in analysis, however the relative pressure signals after the null correction and normalization were extremely repeatable, making such a correction unnecessary. As such, the thermocouple was only used to ensure the FIG did not exceed its operating temperature.

Next, argon was passed through mass flow controller and the anode, causing the FIG and cold-cathode readings to increase until a steady-state gas-load pressure was reached. The stepper motor was then actuated by the micro-controller to rotate the anode assembly one complete revolution while the oscilloscope recorded data. For each sweep, the FIG was

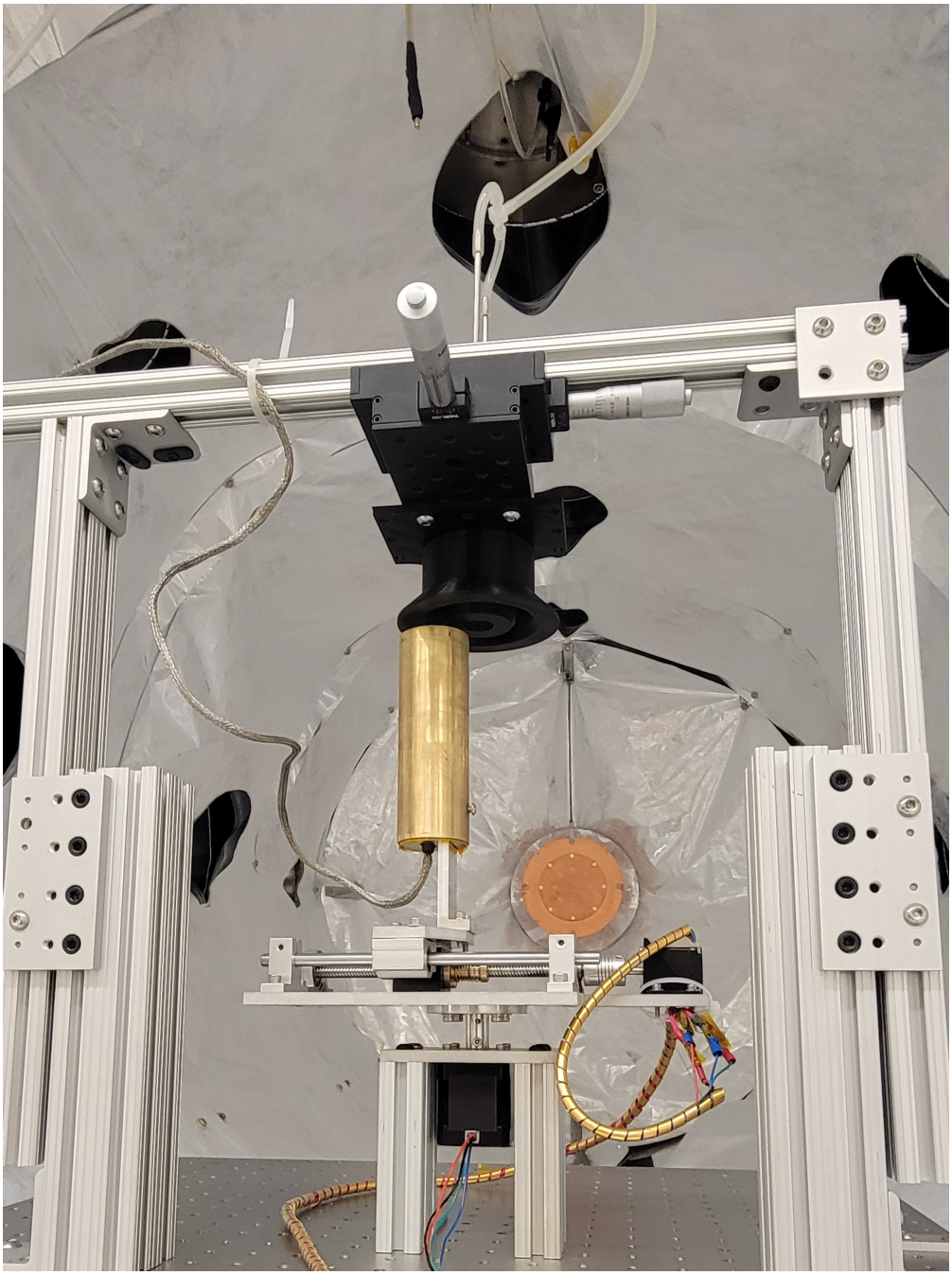

Figure 5.4: The original approach to the apparatus, with the modified FIG mounted on a stage that could both rotate the diagnostic azimuthally as well as radially in the static replica channel.

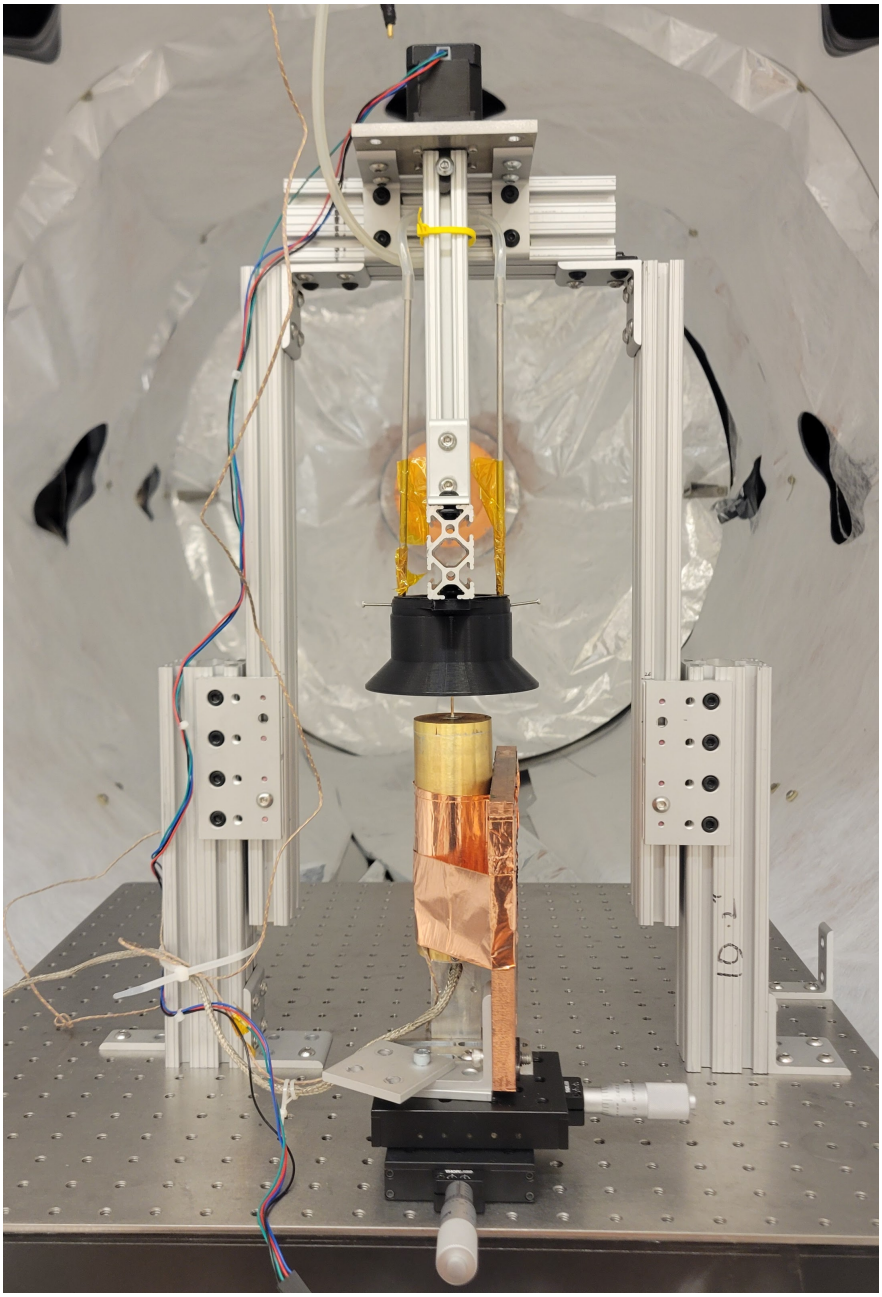

Figure 5.5: The final iteration of the pressure testing apparatus. The FIG is fixed and heat sunk to the large copper block, while the anode/channel assembly hangs and rotates through stepper motor actuation. The anode is obscured in this image, but its gas feed tubes are visible.

initially located 90° azimuthally from both of the gas feed tubes. A reverse revolution followed each initial revolution to return the anode assembly to the initial position, preventing the tangling of the gas feed tubes and FIG cable with the apparatus. After returning to the original azimuthal location, the gas was shut off until a new quasi-steady 'null' pressure reading was reached. The process was repeated three times at a mass flow rate of 10 sccm for each axial location so that the repeatability could be verified, and was conducted a single time for flow rates of 20 sccm and 30 sccm. After measurements for one axial location were completed, SPECTER was brought back up to atmosphere and the anode assembly was placed at the next axial position. This was conducted for four to five axial positions before the anode model was replaced for a different geometry to be tested.

As touched on previously, the modified FIG only began operating reliably after extensive troubleshooting and the disabling of actuated motion capability beyond one cylindrical dimension ($\hat{\theta}$). Rather than invest time into actuated axial motion of the FIG or anode assembly and potentially introduce new problems with the FIG, axial actuation was done manually. This required that in addition to the swapping of anodes, vacuum cycling of SPECTER was necessary for the altering of axial position. Essentially, the accuracy and reliability of the measurements was prioritized at the expense of axial resolution.

Figure 5.6 shows a close-up image of the modified FIG positioned for flow testing.

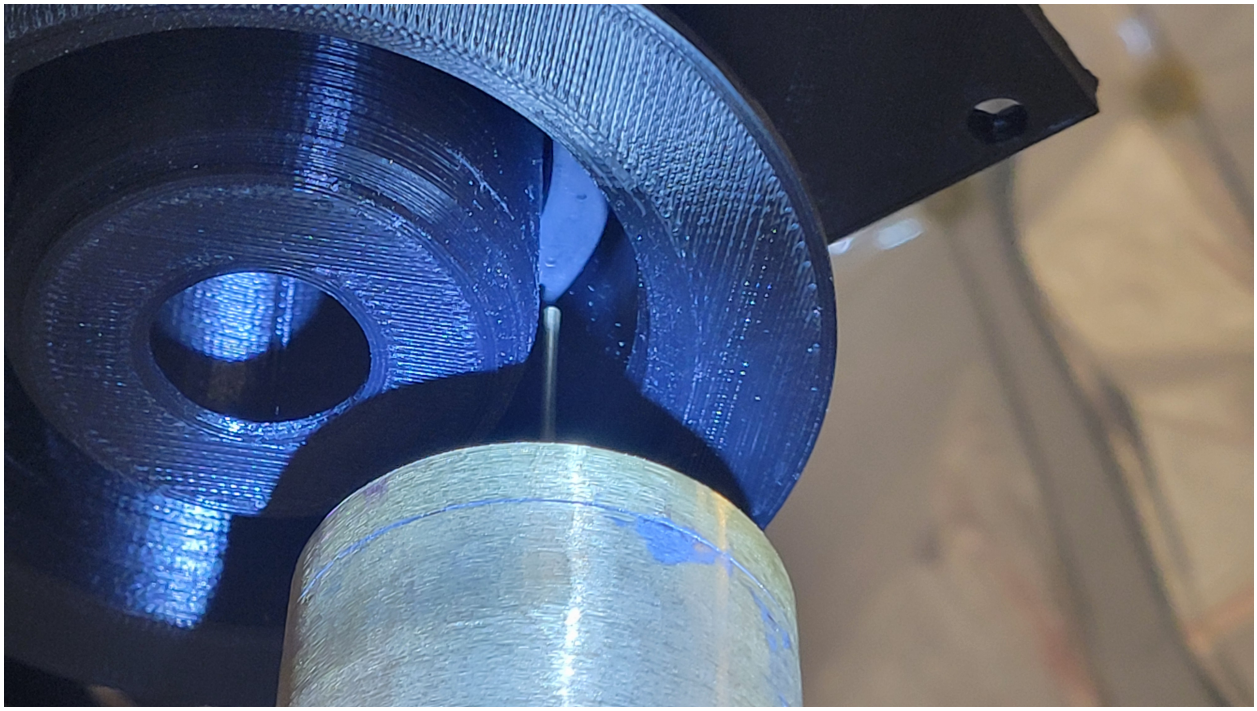

Figure 5.6: The modified FIG positioned in the ACME thruster replica channel downstream of a test anode.

Chapter 6

RESULTS & DISCUSSION

6.1 Flow Measurements

Data from the azimuthal sweeps of the FIG at the tested axial locations are shown in Figures 6.1-6.4. The y-axis of each plot represents the axial position of the FIG inlet for a given sweep, and the mean of each sweep is placed at the axial location of the FIG for that sweep. The scale of each signal is consistent across sweeps for all anodes in Figures 6.1-6.4 so that relative comparisons can be interpreted visually, however the signal variation within individual sweeps is unrelated to the axial position. The axial positions tested were z = 1, 6, 16, and 26 mm from the face of each anode, and an additional location of z = 10 mm was tested for A1. These locations on the plot are expressed as z positions normalized by the channel length from the anode face to the exit plane, L = 26mm. The gas feed tubes were located at the -90° and 90° azimuthal locations, which are labeled. Percentages to the right of each trace correspond to the peak-to-peak deviation from the mean μ for the adjacent axial location.

6.1.1 A1

In Figure 6.1, azimuthal uniformity clearly increases with axial distance from the anode, as deviations from the mean vanish with increased z/L. The measurements for A1 capture the two periodic features that were expected based on the design: 20 distinct maxima corresponding to the exit orifices, as well as two broad peaks centered around or near the -90° and 90° locations. These broad peaks reveal that insufficient mixing occurred within the anode before exiting from the 20 orifices. Figure 6.5 shows the individual azimuthal sweeps for A1 at each axial location, except the y-axis scaling is variable to highlight minute features in

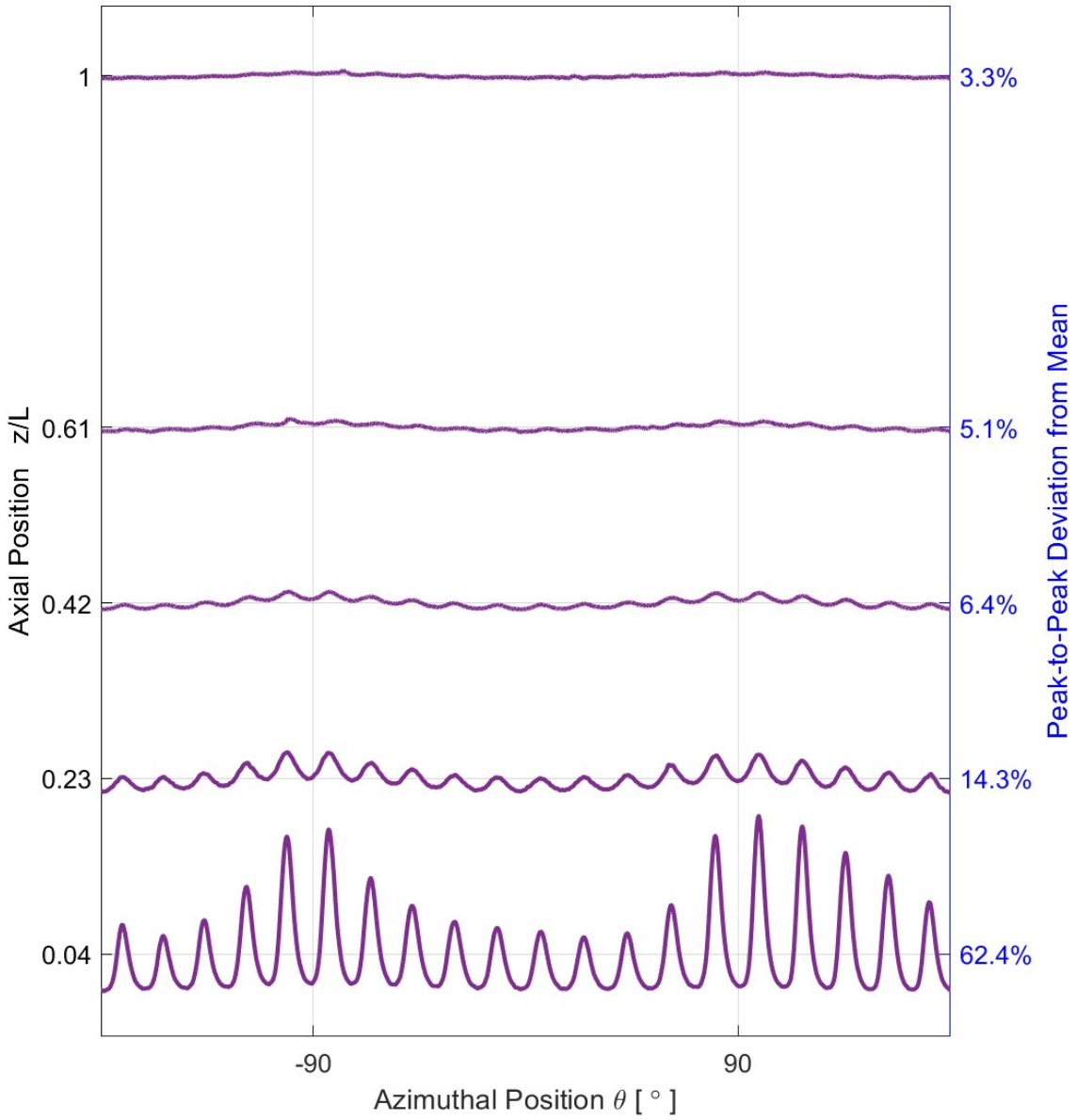

Figure 6.1: A1 pressure data.

downstream measurements. While the magnitude of the pressure changes corresponding to the exit orifices decrease, the broad maxima associated with the gas inlet locations persist and become the dominant component of non-uniformity as the axial distance increases. This axially persistent non-uniformity appears to explain the non-axisymmetric erosion witnessed on ACME surfaces after use of this anode (Figure 3.2). Note that while slight errors in alignment may partially explain the asymmetry of the sweeps across about $\theta = 0°$, it is more plausibly explained by asymmetries in the exit orifices. A close inspection of Figure 3.3 reveals that the 20 orifices are not exactly centered about the central axis of the anode, which would result in greater pressure measurements for the side of the anode with orifices closer to the anode centerline.

6.1.2 A2

The relative pressure characterizations for A2 are shown in Figure 6.2. As intended, the profiles for this mock anode were extremely non-uniform for all axial locations, with a peak-to-peak pressure deviation of $\mu = 28.8\%$ at the exit plane. Thus, this anode design would not meet the standard criteria for an anode with an acceptable level of azimuthally non-uniform propellant injection. The measurement at $z/L = 0.04$ exits the window of the plot due to the extreme relative magnitude at θ positions near the single orifice. That sweep also exhibits an asymmetry near the exit orifice at $\theta = 0°$ that is suspected to result from the confluence of three sources: the measurement time associated with the modified FIG pitot assembly, the relatively massive jump in pressure encountered by the FIG while entering the direct flow of gas, and the direction of motion over the orifice. While not shown, pressure data was recorded during the reverse direction phase of the test procedure for each sweep. Every reverse sweep appeared as a near mirror image of the forward sweep, however the reverse sweep for A2 at $z/L = 0.04$ was the same asymmetric shape as the forward sweep. This asymmetry indicates that gas enters the FIG chamber more rapidly than it exits when transitioning from near the orifice to directly over it. Dotted red lines in Figure 6.2 represent the angular width of the orifice, highlighting this directional observation. For

the downstream sweeps, the apparent impact of sweep direction subsides significantly.

6.1.3 A3

Measurements for A3 are shown in Figure 6.3. The peak-to-peak deviation from the mean was lower for all axial positions than both A1 and A2, and the axial rate of decrease in deviation was substantially lower as well. The three measurements furthest from the face indicate near complete azimuthal uniformity in pressure with peak-to-peak deviation values below 2%. The measurements near the anode face clearly depict the 48 gas exit locations, as well as a larger θ-scale non-uniformity in the profile that is most evident in the general maxima around $\theta \approx 135°$. An apparent maxima suggests that the internal baffles incompletely distribute the gas, and its occurrence at a θ location that is divisible by 45° indicates that the first baffle is where incomplete distribution occurs. The reasoning for this is that the first baffle divides the flow from the two inlets to four evenly spaced orifices that are offset from the inlets at 45°. The plots in Figure 6.5 at the two middle axial locations further reinforce this determination, as four peaks in the two center sweeps are visible at $\theta \approx [\pm 45°, \pm 135°]$. Nevertheless, the A3 exit plane sweep contains no distinct modes of azimuthal non-uniformity, and was the sweep with the most uniform pressure across all anodes and axial positions with $\mu = 0.7\%$.

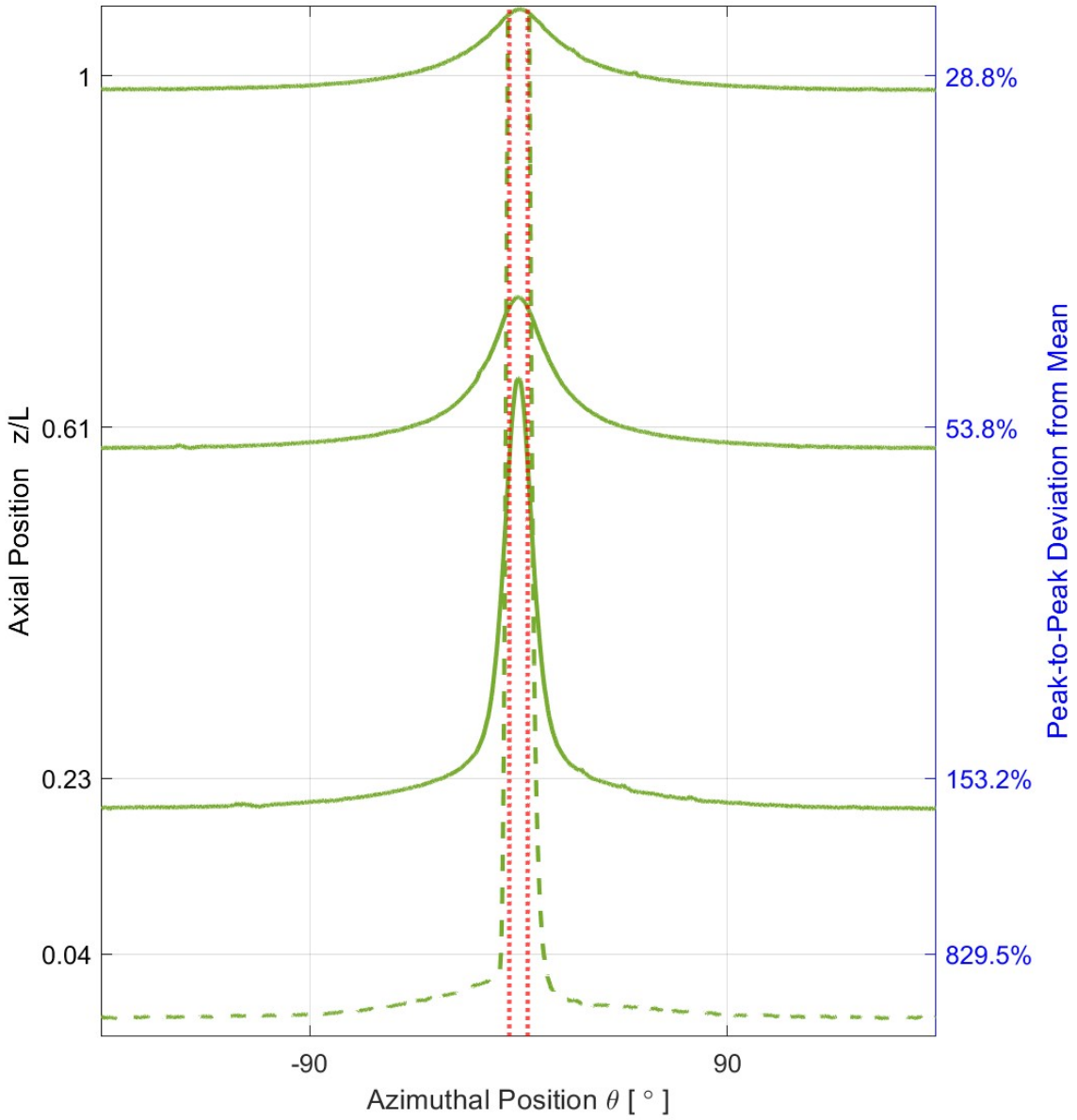

Figure 6.2: A2 pressure data. The dotted red lines show the width and location of the single exit orifice.

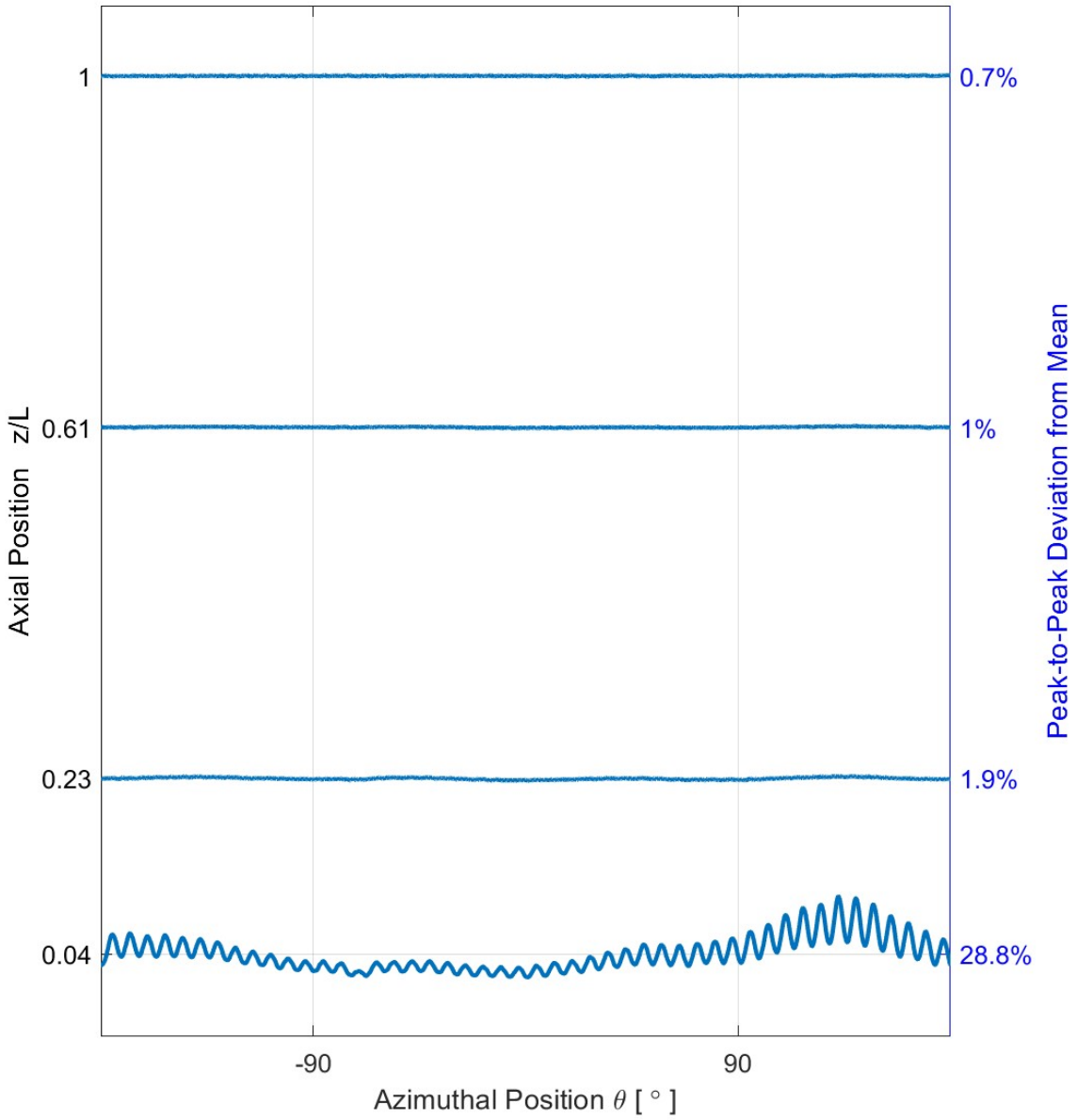

Figure 6.3: A3 pressure data.

6.1.4 A4

Results for A4 show that the design exhibits generally uniform gas injection, with the maximum peak-to-peak pressure deviation of 2.8% for the near-anode sweep. The average magnitude of absolute pressure at $z/L = 0.04$ was lower than that at $z/L = 0.23$, which was the solitary case of average absolute absolute pressure increasing with axial distance from the anode. Absolute pressure measurements for all other anodes and the three other differences for A4 exhibited decreases in absolute pressure, as is generally predicted from prior experiments and HPHALL-2 simulations [28]. It is suspected that the unique decrease is due to the radial gas injection of A4 in conjunction with the axially aligned pressure probe. The modified FIG inlet orifice was essentially obscured from the bulk flow direction of particles.

With the consistent scaling used in Figures 6.1 - 6.4, non-uniformities in A4 are nearly indistinguishable. With the finer scale provided in Figure 6.5, it is seen that there is a distinct structure to the $\sim$ 1-2% peak-to-peak deviation from the mean, with a maxima occurring near $\theta = 135°$ and a minimum near $\theta = 10°$. As there is no consistent, evenly spaced pattern to the non-uniform structure of the pressure profiles, the same reasoning applied to the non-uniformities of A3 is not valid. Furthermore, improper or skewed alignment of the anode relative to the FIG is unlikely to have caused this non-uniformity because due to symmetry, the signal would be generally sinusoidal about the mean for all θ. Instead, a sinusoidal shape in the pressure profiles for the two upstream locations extend only half of the θ range. The sweep at $z/L = 1$ appears to have a very low magnitude sinusoidal structure across the entire azimuthal range that may stem from some slight skew in alignment, although the periodic fluctuation is within the bounds of uncertainty of the FIG. It may be that the relative pressure minimum and maximum near $\theta \approx 5°$ and $\theta \approx 135°$ can be explained by errors in the manufacturing process that produced channels of asymmetrical gas conductance, causing preferential flow rates in some azimuthal regions. Despite this, the neutral flow uniformity is still well within the bounds of acceptance from prior Hall thruster research.

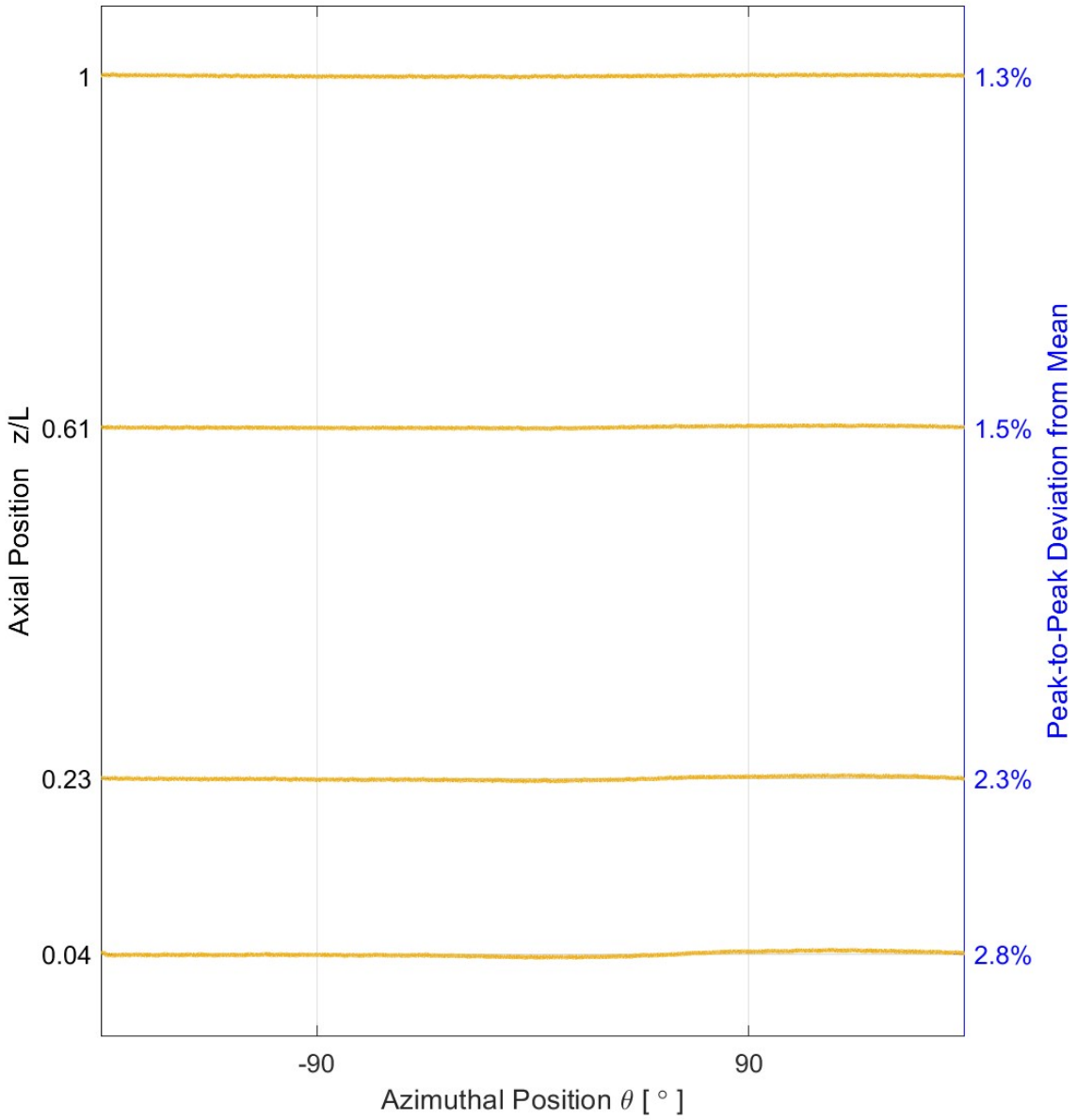

Figure 6.4: A4 pressure data.

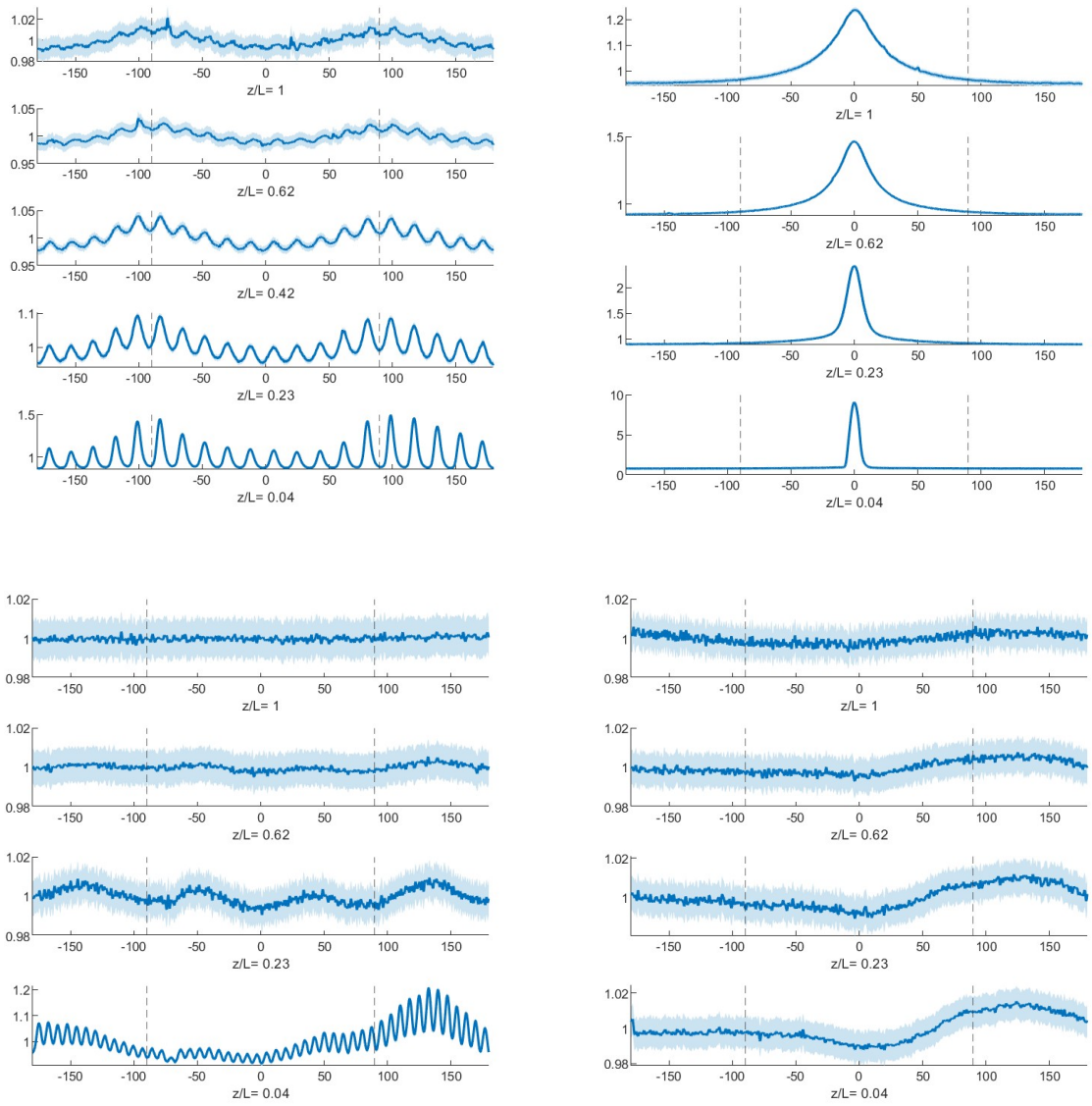

Figure 6.5: Pressure data with variable scaling for every sweep, not spaced according to axial position. Top left: A1. Top right: A2. Bottom left: A3. Bottom right: A4.

6.1.5 Uncertainty

The absolute uncertainty in FIG pressure measurements was substantial, partially due to thermal baseline drift. When the FIG was quickly turned off and back on again while measuring a constant pressure, the quasi-steady reading would shift in magnitude. However, the repeatability of sweeps after normalization was excellent, meaning the relative uncertainty between sweeps was very low. This uncertainty condition was acceptable since the experimental objective was to quantify uniformity, or relative fluctuations about a mean measurement. In Reid's extensive characterization of Hall thruster neutral flow dynamics, a nearly identical situation is described regarding uncertainty, although the diagnostic used in that case was a Pirani gauge [28]. The maximum relative error between a data point of a single theta location on a smoothed sweep and the mean for three identical sweeps was 2.72%, with the average error between an individual sweep and the mean for that condition being 0.19%.

6.2 Summary of Uniformity Acceptance Results

Quantitative assessment of azimuthal pressure uniformity for the four anode designs was done with three metrics: the peak-to-peak deviation from the mean, the maximum absolute deviation from the mean, and the standard deviation. The first two are used in existing research that this experiment was modeled on, while the standard deviation provides additional insight. Each azimuthal sweep was assessed for the three metrics at argon flow rates of 10, 20, and 30 sccm through the anodes. The values for different flow rates were averaged at each axial position, and with these averages exponential fitting functions were made of the form

$$g(z/L) = Ae^{-B(z/L)} + Ce^{-D(z/L)}. \tag{6.1}$$

Figures 6.6 - 6.8 depict the data and fits for the three metrics and criteria while Tables 6.1 - 6.3 contain the fit functions and axial positions where acceptance is satisfied. The two

criteria from the literature reference are evaluated at the $z = L/2$ location, making the lower left quadrant formed by the two dashed red lines the 'zone of acceptance'. For the standard deviation σ, prior research does not suggest a threshold for acceptable anodes. Given that a sine wave centered at 1 and with amplitude 0.05 meets both of the criteria from literature, it follows that the standard deviation of such a wave, 3.54%, would be an reasonable threshold for σ. Values corresponding to $z = L/2$ are also included in Tables 6.1 - 6.3.

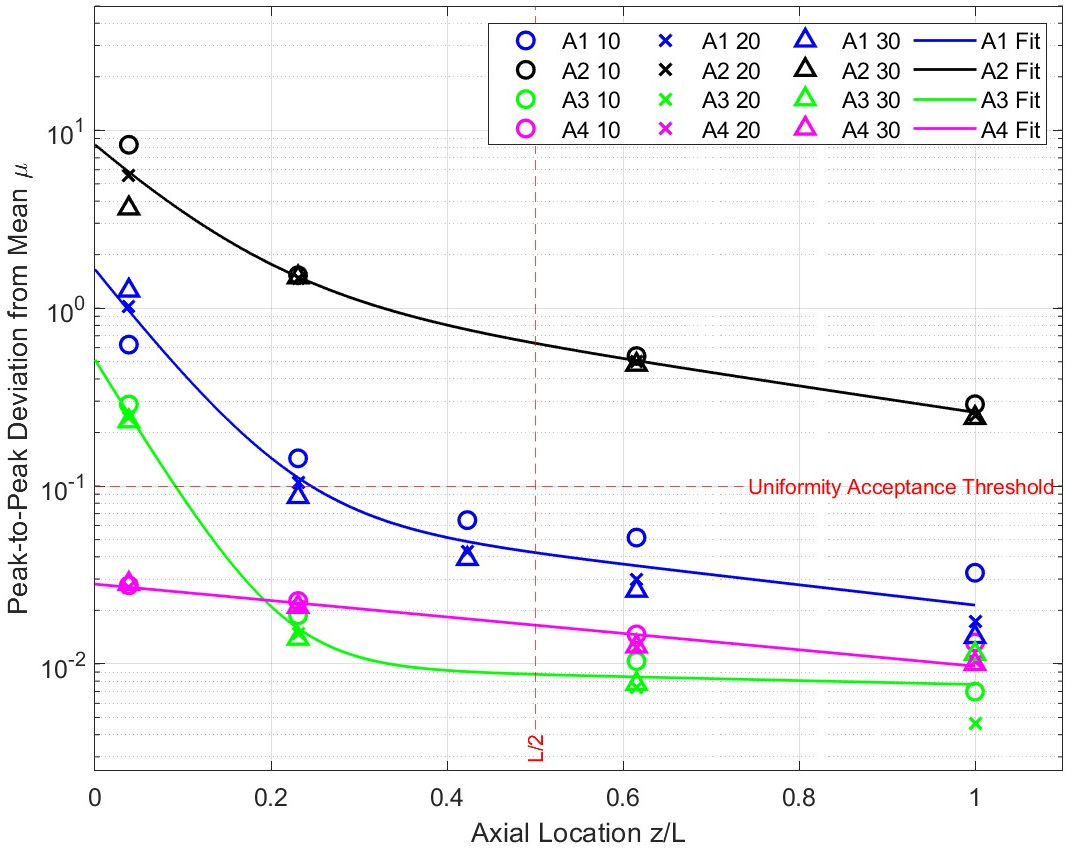

Figure 6.6: Peak-to-peak deviation from mean (μ) for all measurements plotted with empirical fit functions. Values next to anode names represent the flow rate in sccm for argon.

Anodes A1, A3, and A4 meet all the criteria, while A2 does not meet any. Critical

Anode	$\mu(z/L)$	$(z/L)_{0,\mu}$	$\mu_{L/2}$
A1	$1.57e^{-14.7(z/L)} + 0.08e^{-1.31(z/L)}$	0.246	4.23%
A2	$0.50e^{-18.8(z/L)} + (9.8 \times 10^{-3})e^{-0.255(z/L)}$	Unattained	63.5%
A3	$6.87e^{-11.0(z/L)} + (1.424)e^{-1.70(z/L)}$	0.0911	0.87%
A4	$0.029e^{-1.28(z/L)}$	Upon Injection	1.65%

Table 6.1: Peak-to-peak deviation from mean (μ) fit functions, evaluation of the fits at $z = L/2$, and the axial locations where the uniformity threshold ($\leq$10%) is attained).

Anode	$\alpha(z/L)$	$(z/L)_{0,\alpha}$	$\alpha_{L/2}$
A1	$1.39e^{-15.9(z/L)} + 0.05e^{-1.34(z/L)}$	0.195	2.57%
A2	$6.72e^{-11.0(z/L)} + 1.33e^{-1.85(z/L)}$	Unattained	55.5%
A3	$0.366e^{-19.78(z/L)} + (5.3 \times 10^{-4})e^{-0.27(z/L)}$	0.068	0.47%
A4	$0.015e^{-1.24(z/L)} + (4.4 \times 10^{-6})e^{5.5(z/L)}$	Upon Injection	0.87%

Table 6.2: Maximum absolute deviation from mean (α) fit functions, evaluation of the fits at $z = L/2$, and the axial locations where the uniformity threshold ($\leq$5%) is attained).

Anode	$\sigma(z/L)$	$(z/L)_{\sigma<3.54\%}$	$\sigma_{L/2}$
A1	$0.29e^{-14.8(z/L)} + 0.023e^{-1.58(z/L)}$	0.189	1.1%
A2	$0.927e^{-12.7(z/L)} + 0.287e^{-1.45(z/L)}$	Unattained	14.1%
A3	$0.10e^{-15.59(z/L)} + (2.1 \times 10^{-3})e^{-1.65(z/L)}$	0.071	0.01%
A4	$(7.36 \times 10^{-}3)e^{-1.07(z/L)}$	Upon Injection	0.43%

Table 6.3: Standard deviation (σ) fit functions, evaluation of the fits at $z = L/2$, and the axial locations where the uniformity threshold ($\sigma \leq 3.54\%$) is attained.

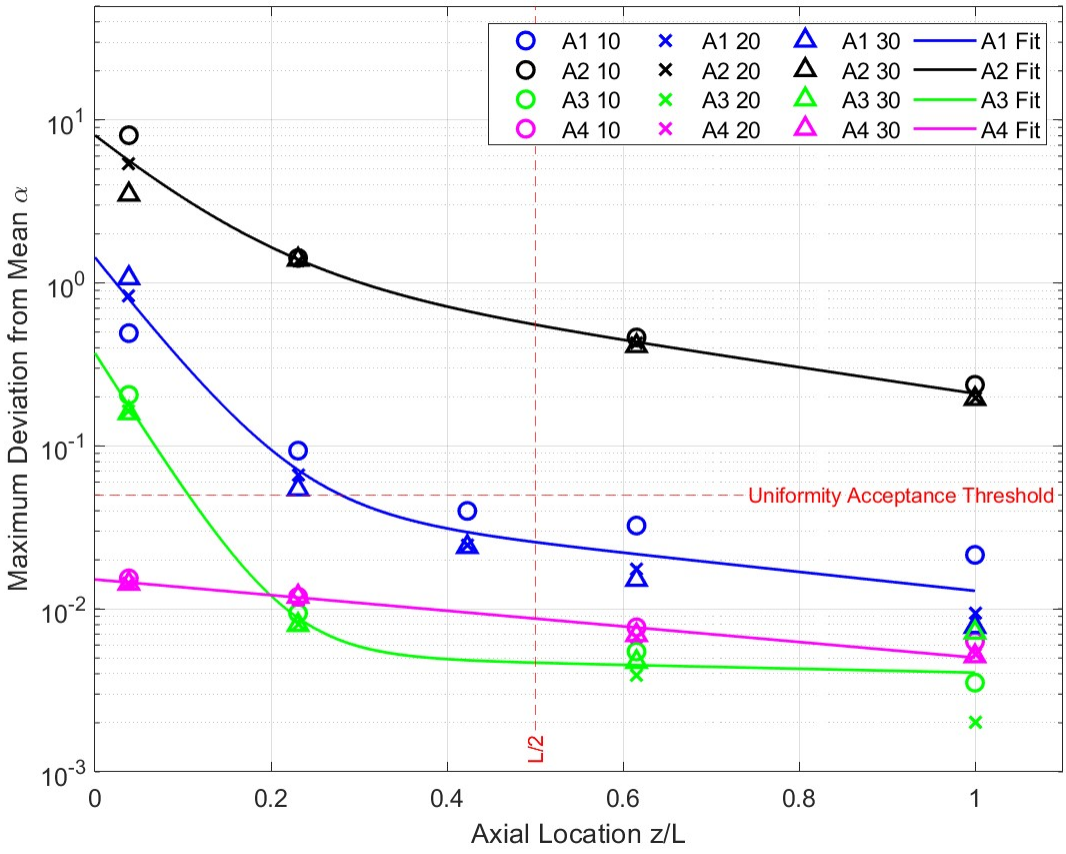

Figure 6.7: Maximum absolute deviation from mean (α) for all measurements alongside empirical fit functions. Values next to anode names represent the flow rate in sccm for argon.

z/L values in tables 6.1 - 6.3 show that the μ criteria is more stringent, as z/L locations where they are met are greater. As intended, A3 and A4 exhibited significantly better flow uniformity than A1, however A1 showed better uniformity than expected. While the result for A1 calls into question the rigor of the experimental methods due to the observed non-uniformities in ACME testing, the trend of uniformity from A1 to A3 and A4 strongly indicate that efforts to improve azimuthal uniformity of gas injection were successful.

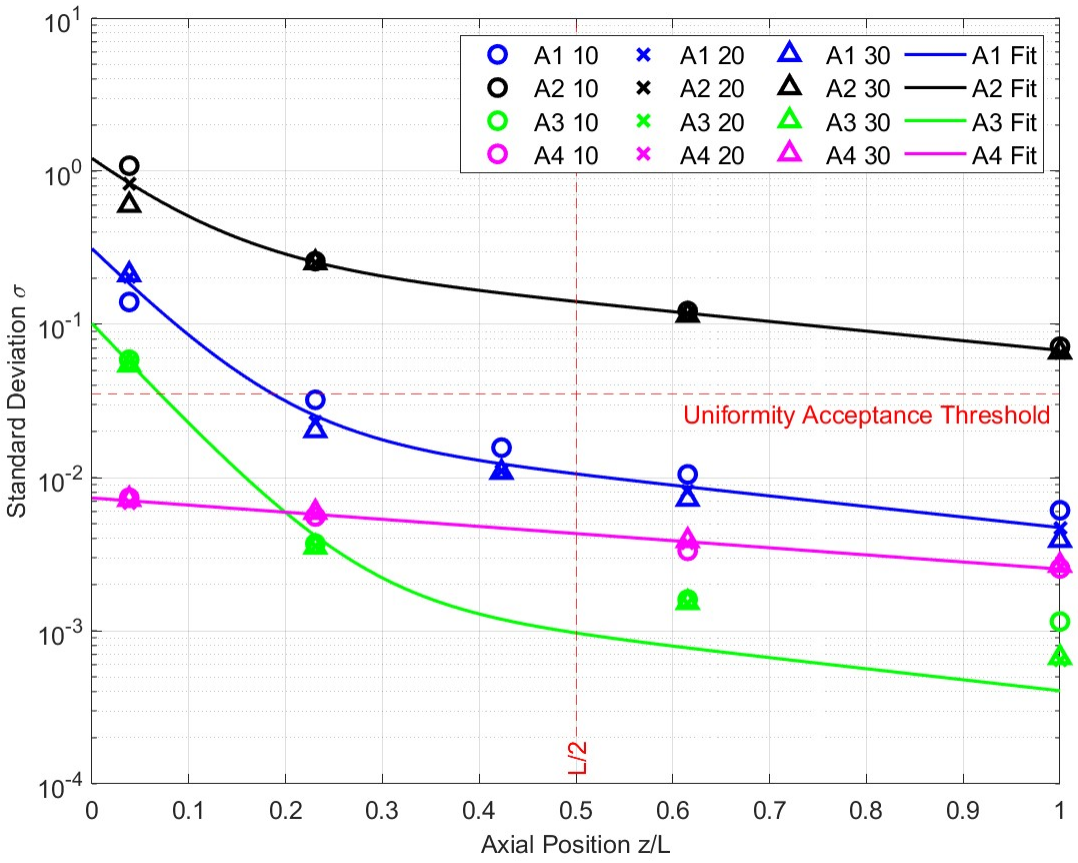

Figure 6.8: Standard Deviation (σ) for all measurements plotted with empirical fit functions. Values next to anode names represent the flow rate in sccm for argon.

Chapter 7

CONCLUSIONS AND FUTURE WORK

7.1 Comparison

A comparison of results for the tested anodes with results from other similar experiments is provided in Table 7.1. Some values for α and μ are approximate as they were estimated visually from figures presented in the relevant publications.

Anode/Thruster	**Gas, Flow Rate [sccm]**	$\alpha_{L/2}$	$\mu_{L/2}$	$\sigma_{L/2}$
H9 SN01 [16]	Xe, 20.3	$\sim 4.2\%$	9.2%	-
H9 SN02	Xe, 20.3	$\sim 2.1\%$	4.6%	-
H9 SN03	Xe, 20.3	$\sim 2.0\%$	4.1%	-
MaSMi-DM SN1 [9]	Xe, 10.2	$\sim 1.5\%$	3.2%	-
MaSMi-DM SN2	Xe, 10.2	$\sim 1.0\%$	1.5%	-
BPT-4000 [12]	-	$\sim 5\%$	$\sim 7\%$	-
ACME (A1)	Ar, 10-30	2.57%	4.23%	1.1%
A2	Ar, 10-30	55.5%	63.5%	14.1%
A3	Ar, 10-30	0.47%	0.87%	0.01%
A4	Ar, 10-30	0.87%	1.65%	0.43%

Table 7.1: Comparison table for APAT results from notable research and this work. Approximate values listed are those interpreted from figures presented in respective source literature. The fact that some reported values have $\mu_{L/2} > 2\alpha_{L/2}$ suggests that the reported $\mu_{L/2}$ may be upper bounds of uncertainty margins.

The comparative results in Table 7.1 suggest that the uniformity of gas injection of the anodes designed for use in ACME is on par with that from state-of-the-art Hall thruster anodes. While tempting to accept this, the unexpectedly uniform result for A1 in particular raises three questions:

1. What metric(s) justify the criteria of $\mu_{L/2} = 10\%$ and $\alpha_{L/2} = 5\%$ set by previous flow-uniformity researchers?

2. Was the non-uniformity in gas injection for ACME testing with A1 substantial enough that it was affecting performance?

3. Was the measurement technique employed in this work rigorous enough to be trusted and compared to the peer-reviewed research from esteemed Hall thruster researchers?

Regarding the first question, it would be useful to collaborate with those who have brought about the standardized acceptance thresholds to understand the reasoning behind them. It could be logically gathered that the established thresholds are the points at which the effects of non-uniformities on ionization and efficiency become negligible, but some quantitative rigor would provide useful insight. A thorough literature review could attempt to discern the origination of the thresholds based on comparisons between performance of different thrusters and their gas injection uniformity, however this may prove unfruitful.

To address the second question, ACME performance tests would have to be conducted under identical operating conditions while using A3 and A4. Testing with A4 is currently underway, so any improvements due to the anodes may be quantified in the near future. The results from performance comparisons for ACME with A1 and ACME with A4 may shed light onto both the validity of the presented gas flow uniformity testing as well as the acceptance threshold significance.

Finally, regarding third question, there are differences between the methods used in this experiment and those in published research that may explain the results of unexpectedly high azimuthal uniformity for A1. The difference that most likely led to bias in results is

that the measurements of anodes in this study were continuous 360° sweeps, while in the experiments of Conversano, Reid, and Hofer et al., discrete θ locations were measured for set durations that ensured steady-state pressure measurements were reached [9] [16] [28]. While the nude FIG in the direct path has a near instantaneous rise time on the order of $5\mu s$, the capsule and pitot probe modification delay the incoming gas from reaching the grid electrode. This necessarily increases the settling time of changes in pressure measurements read by the FIG, in exchange for gains in spatial resolution. The pressure sensing settling time is determined by Conversano et al. with the standard equation for vacuum conductance and an approximation:

$$\tau_{\Delta p} = \frac{V_{gauge}}{S_{eff}} \log(\frac{P_0 + \Delta P}{P}) \approx \frac{V_{gauge}}{\pi v_{th} d^3/(12 L_p)} \log(\frac{P_0 + \Delta P}{P_0}) \tag{7.1}$$

where V_{gauge} is the internal volume of the gauge, S_{eff} is the effective conductance, d is the pitot tube diameter, L_p is the overall pitot tube length, v_{th} is the mean thermal velocity and P_0 is a reference pressure [9] [11]. Molecular flow is assumed in this method due to Knudsen numbers of 4-40 for the pressure range of 1×10^{-3}-1×10^{-2}, although Reid [28] and Huang et al. [18] found that the Knudsen number is ~ 1 in the near anode region of Hall thruster channels. Using m = m_{Ar} in Equation 2.9 and inserting values from the apparatus of this experiment yields a 10% pressure difference settling time of

$$\tau_{10\%\Delta p} \approx \frac{1.15 \times 10^{-4} \text{ m}^3}{\pi(386 \text{ m/s})(1.7 \times 10^3 \text{ m})/(12 \cdot 0.038\text{m})} \log(1.1) = 0.88 \text{ s}. \tag{7.2}$$

According to this calculation, around one second should be allocated per 10% change in pressure in order to obtain steady-state measurements from the modified FIG. Since the FIG was rotated continuously for these tests, and at times the derivative of pressure readings exceeded 10% per second, the results presented likely underestimate deviations from the mean. This would explain, at least partially, the unexpectedly uniform pressure profile for A1 and the extreme uniformity of the A3 and A4 versus those from esteemed research groups. However, the rate of deviation for measurements far from the anode face

were generally much less than 10% per second, meaning that the potential error from not allowing sufficient measurement time would be lower for those axial positions (including $L/2$).

While the choice to continuously rotate the FIG for data collection was not as accurate for determining the relative pressure magnitudes, it provided higher angular resolution (50,000 measurements per 360°) than results presented in similar work. Fine structures in the pressure profiles as seen in Figures 6.1 and 6.2 would have been obscured with discrete measurement points. To attain measurements of high accuracy and fine spatial resolution, the rotation of the FIG could have been slowed, however the software package used to operate the rotational stepper motor was limited by a lower bound for the driving of angular speed.

7.2 Improvements to Methods and Future Work

Numerous improvements and adjustments to the methods used for Hall thruster anode gas flow characterizations should be made going forward with this work.

7.2.1 Procedural Improvements

Slowing the rate of probe rotation during the continuous data collection sweeps to account for the full settling time of the pitot modification would improve the accuracy of relative pressure measurements. Since these measurements dictate the acceptance of an anode design, their accuracy is essential for quantifying magnitudes of non-uniformities.

7.2.2 Apparatus Improvements

Potential effects of interaction of the main FIG body with the gas flow through the anode/channel assembly could be mitigated by bending the pitot tube at a 90° angle and extending it such that the diagnostic itself is not in the direction of flow. This tactic was used in the references that guided this experiment, however the extent to which this affected results was not quantified [9] [16] [28].

As indicated by Equation 7.1, the volume of the FIG capsule and the pitot tube length should be minimized to keep the pressure sensing settling time as low as possible. The diameter of the pitot tube d will also affect the settling time, but a choice in d will depend on the desired spatial resolution, while V_g and L_p are independent of resolution.

The selection of materials and design for the FIG modification resulted in a manageable but persistent amount of thermal drift in measurements. Improving the thermal management of the FIG so that a thermal steady state is achieved would improve accuracy and mitigate the need for corrections. Also, including either a semi-transparent material or 'window' for part of the FIG assembly would be useful for knowing whether the FIG filament is operating properly.

Additional actuators would drastically reduce the amount of time required to obtain data from this experimental apparatus. A majority of the testing time was spent cycling SPECTER from vacuum to atmosphere and back to facilitate manual axial positioning. Actuators permitting motion in the axial and radial directions would theoretically rid the need for any vacuum cycling as well as greatly enhance pressure characterization capabilities.

Quantifying the soundness of comparing gas flow through anodes of different materials was intended to be addressed in this work, but ultimately was not due to time constraints. Comparing anodes of the same material would improve the scientific robustness of the presented experiments overall, and comparing two anodes of identical design but different material would give insight into material effects.

7.2.3 ACME Performance Testing and Erosion

Testing of the ACME thruster equipped with the A4 anode is currently underway. While the focus of present test campaigns do not relate directly to anode manipulation and the effect that uniform gas injection has on thruster performance, future campaigns may target that information. Optimization of anode geometry and other anode modifications were presented in Thoreau's general exam [32] and can are anticipated to be included in the dissertation that will follow. As a preliminary result of this work, Figure 7.1 shows the ACME thruster after

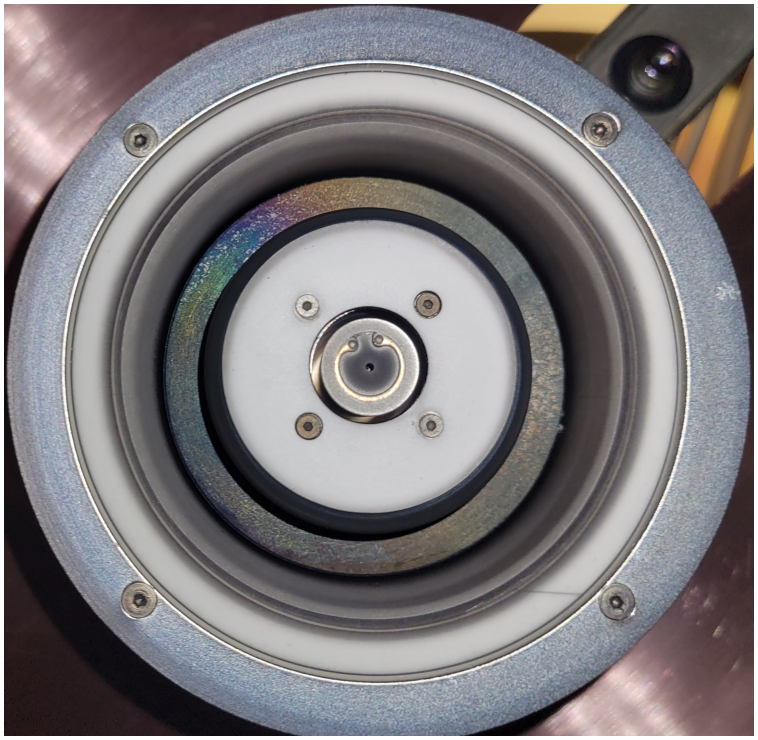

Figure 7.1: ACME after ∼30h of testing with the stainless steel A4 anode. White eroded surfaces are mostly axisymmetric, particularly in comparison to Figure 3.2.

∼ 30 hours of testing with the stainless steel A4 anode. The erosion pattern on the outer insulation is highly axisymmetric compared to that seen in Figure 3.2, potentially indicating improved propellant density uniformity.

Given the vast parameter space of Hall thruster operation and the continuously changing conditions and personnel in the SPACE Lab, it may never be definitive whether the increased azimuthal uniformity of flow through the novel anodes improves the performance of the ACME thruster. Nevertheless, the experimental and analytical processes used in the execution of this project have prepared the author for yet greater and more fruitful projects to come.

BIBLIOGRAPHY

[1] Protolabs: Direct metal laser sintering. https://www.protolabs.com/services/3d-printing/direct-metal-laser-sintering/. Accessed on: May 15, 2024.

[2] Protolabs: Multi jet fusion. https://www.protolabs.com/services/3d-printing/multi-jet-fusion/. Accessed on: May 15, 2024.

[3] Arun Microelectronics. Ion gauge schematic. https://arunmicro.com/news/how-does-an-ion-gauge-work/.

[4] Vladimir Baranov, Yuri Nazarenko, and Valery Petrosov. Azimuthal non-uniformities in accelerators with closed electron drift. IEPC 2001-018. Presented at the 27th International Electric Propulsion Conference, Pasadena, California, USA, Oct 2001.

[5] Beam Dynamics, Inc. *Model FIG-1 Fast Ionization Gauge Instruction Manual*. Eden Prairie, Minnesota 55344, USA, February 2001.

[6] Gabriella Blackner. Back to the moon: Aeps and lunar gateway mission. Talk/Lecture, May 2023. Chief Engineer, Advanced Electric Propulsion System (AEPS).

[7] Carl F. Book and Mitchell L.R. Walker. Effect of anode temperature on hall thruster performance. *Journal of Propulsion and Power*, 26:1036–1044, 2010.

[8] Ryan Conversano, Robert Lobbia, Thomas Kerber, Kimberlyn Tilley, Dan Goebel, and Sean Reilly. Performance characterization of a low-power magnetically shielded hall thruster with an internally-mounted hollow cathode. *Plasma Sources Science and Technology*, 28, 10 2019.

[9] Ryan W Conversano, Dan M Goebel, Ira Katz, and Richard R Hofer. Low-power hall thruster with an internally mounted low-current hollow cathode, 7 2020. US Patent 10,723,489 B2, California Institute of Technology, Pasadena, CA.

[10] Ryan W Conversano, Dan M Goebel, and Richard E Wirz. Magnetically shielded miniature hall thruster. https://patents.google.com/patent/US20150128560A1/en, 5 2015. Patent Application Publication.

[11] Ryan W Conversano, Robert B Lobbia, Thomas V Kerber, Kimberlyn C Tilley, Dan M Goebel, and Sean W Reilly. Performance characterization of a low-power magnetically shielded hall thruster with an internally-mounted hollow cathode. *Plasma Sources Science and Technology*, 28(10):105011, oct 2019.

[12] Kristi deGrys, Nicole Meckel, George Callis, Doug Greisen, Andrew Hoskins, David King, Fred Wilson, Lance Werthman, and Vadim Khayms. Development and testing of a 4500 watt flight type hall thruster and cathode. pages 15–19, 11 2001. IEPC 2001-011. Presented at the 27th International Electric Propulsion Conference, Pasadena, California, USA, Oct 2001.

[13] Dan M. Goebel and Ira Katz. *Fundamentals of Electric Propulsion*. Wiley, 2nd edition, 2023.

[14] R. J. Goldston and P. H. Rutherford. *Introduction to Plasma Physics*. CRC Press, 1995.

[15] Daniel A. Herman, Timothy Gray, Ian Johnson, Taylor Kerl, Ty Lee, and Tina Silva. The application of advanced electric propulsion on the nasa power and propulsion element (ppe), 2019. Presented at the 36th International Electric Propulsion Conference, University of Vienna, Vienna, Austria, September 15-20, 2019.

[16] Richard R. Hofer, Sarah E. Cusson, Robert B. Lobbia, and Alec D. Gallimore. The h9 magnetically shielded hall thruster. https://electricrocket.org/2019/651.pdf, 2017. Presented at the 35th International Electric Propulsion Conference, Georgia Institute of Technology, Atlanta, Georgia, USA, October 8-12, 2017.

[17] Richard Robert Hofer. *Development and Characterization of High-Efficiency, High-Specific Impulse Xenon Hall Thrusters*. PhD thesis, 2004.

[18] Wensheng Huang, Alec D. Gallimore, and Richard R. Hofer. Neutral flow evolution in a six-kilowatt hall thruster. *Journal of Propulsion and Power*, 27:553–563, 2011.

[19] Beam Dynamics Inc. Beam dynamics inc. https://www.beamdynamicsinc.com/. Accessed: 2024-05-26.

[20] Robert G Jahn. *Physics of Electric Propulsion*. Dover Publications, 1996.

[21] Vladimir Kim, Vyacheslav Kozlov, Alexei Lazurenko, Alexander Skrylnikov, Konstantin Kozubsky, and Michel Lyszyk. *Investigation of the anode configuration influence on the PPS-1350 laboratory model plume divergence*.

[22] Naoya Kuwabara, Masatoshi Chono, Naoji Yamamoto, and Daisuke Kuwahara. Electron density measurement inside a hall thruster using microwave interferometry. *Journal of Propulsion and Power*, 37(3):491–494, 2021.

[23] Qi Liu, Yong Li, Yanlin Hu, and Wei Mao. Effects of magnetic field gradient on the performance of a magnetically shielded hall thruster. *Aerospace*, 10(11), 2023.

[24] Shixu Lu, Liexiao Dong, Wei Luo, Shengtao Liang, Jianfei Long, Xiaocheng Zhu, Ning Guo, and Luxiang Xu. Review of closed drift thruster neutral flow dynamics. *AIP Advances*, 13, 7 2023.

[25] Ioannis G. Mikellides, Ira Katz, Richard R. Hofer, and Dan M. Goebel. Magnetic shielding of walls from the unmagnetized ion beam in a hall thruster. *Applied Physics Letters*, 102, 1 2013.

[26] MKS Instruments. Glass bayard-alpert ionization vacuum gauge. https://www.mks.com/f/274-glass-bayard-alpert-ionization-vacuum-gauge.

[27] A. Olano, J. Ren, G. Zhang, H. Tang, T. Zhang, and J. Li. Improvements in miniaturized hall thrusters by use of high-temperature smco magnets and additive manufacturing techniques. volume 576. Institute of Physics Publishing, 8 2019.

[28] Bryan Reid. *The Influence of Neutral Flow Rate in the Operation of Hall Thrusters.* PhD thesis, 01 2009.

[29] Bryan M. Reid. Review of hall thruster neutral flow dynamics iepc-2007-038. 2007.

[30] M Alberto Rossi. *Développement d'outils d'optimisation dédiés aux circuits magnétiques des propulseurs à effet Hall.* PhD thesis, 2017.

[31] Teledyne Hastings Instruments. Ion gauges. Online document. Available at: https://mmrc.caltech.edu/Vacuum/Teledyne

[32] Peter Thoreau. Influence of field topology on magnetically shielded hall thruster operation. General exam, June 2023.

[33] Guojun Xia, Hong Li, Yongjie Ding, Liqiu Wei, Shaowen Chen, and Daren Yu. Performance optimization of a krypton hall thruster with a rotating propellant supply. *Acta Astronautica*, 171:290–299, 2020.

[34] Y. Yashnov, J. McVey, C. McLean, and Edward Britt. Influence of azimuthal nonuniformities on hall thruster operation. 07 2001. Presented at the 27th Joint Propulsion Conference and Exhibit.